Capturing particle-fluid heat transfer in thermo-hydro-mechanical analyses using DEM coupled with a pore network model

Tokio Morimoto[1,2*], Catherine O'Sullivan[2], and David M. G. Taborda[2]

[1.]Department of Civil Engineering, The University of Tokyo, Japan

[2.]Department of Civil and Environmental Engineering, Imperial College London, UK

*Corresponding author: morimoto@civil.t.u-tokyo.ac.jp

Keywords: Discrete element method; Computational fluid dynamics; Pore Network Modelling; Nusselt number; Graetz problem; Granular materials

Abstract

Numerical simulation of fluid-saturated granular materials subject to temporal or spatial variations in temperature is important for a range of industrial applications and to understand a number of natural processes. Amongst the available fluid-coupling options for Discrete Element Method (DEM), pore network models (PNMs) are attractive as the local heterogeneities in the flow field can be captured with a relatively low computational cost. Any coupled DEM-PNM framework that considers thermal behaviour must account for heat transfer between the solid particles and the fluid phase. This contribution develops a novel expression for the Nusselt number for use in coupled DEM-PNM formulations. Previous studies considering Nusselt number formulations for flow in pipes formed the basis for the proposed model. Finite volume simulations of laminar fluid flow through assemblies of spheres were used to assess the model's efficacy and to calibrate the empirical parameters.

Introduction

This contribution addresses the challenge of modelling heat transfer between the solid and fluid phases in a saturated particulate material with laminar fluid flow using a discrete element method (DEM) code coupled with a pore network model (PNM). The DEM-PNM approach is significantly more computationally efficient than coupling approaches that fully resolve the flow in the pore space. Previous studies have demonstrated that accurate predictions of overall permeability and local flow can be made provided that the granular medium is stress transmitting or percolating (not dilute) and appropriate consideration is given to the conductance term that quantifies the loss of energy along individual pore throats (Chareyre et al., 2012; Sufian et al., 2019; Morimoto et al., 2022). Modelling particle-fluid interactions for systems that conduct heat or that are subject to temperature change is important for many applications e.g. geothermal energy and packed bed energy storage. Caulk et al. (2020) showed that a coupled DEM-PNM modelling framework can be adapted to simulate thermal behaviour. Such models need to capture advection and conduction of heat. Here advection refers to the heat transfer phenomena where there is a simultaneous transfer of heat and movement of material, i.e. the pore fluid. Heat transfer takes place between the pore fluid and the particles as well as through the pore fluid. Amongst these mechanisms, modelling the particle-fluid heat transfer term poses the biggest challenge due to the complex geometry of the pore space existing in granular materials. This contribution considers how to model particle-fluid heat transfer in a DEM-PNM framework so that a DEM-PNM network can simulate both advection and conduction accurately.

Caulk et al. (2020) proposed a thermally coupled PNM using a fluid-particle conduction model that considers the overall Reynolds number of the flow in the system and the global solid fraction following Gunn (1978) and Tavassoli et al. (2015). The current study develops upon these contributions with an emphasis on capturing the local advection of heat and fluid-particle conduction along the individual pore throats that map to the edges in the PNM. The model draws on studies that have considered wall-fluid heat transfer in pipes.

In a saturated granular material where the pore fluid is not stationary, a coupled DEM-PNM modelling framework must be able to capture particle-particle heat conduction (e.g. Feng, et al. (2009); Yun and Evans (2010); Morimoto et al. (2022a)), but also pore fluid conduction, pore fluid advection and particle-fluid heat transfer (Yun and Santamarina, 2008). Neglecting viscous dissipation, heat transfer in the pore fluid can be described using an energy transport equation that includes a term, η, representing the energy input to the fluid per unit volume via particle-fluid heat transfer as follows:

$$\rho_f c_f \frac{\partial T}{\partial t} + \rho_f c_f (\boldsymbol{u} \cdot \nabla T) = \nabla \cdot \left(k_f \nabla T\right) + \eta \qquad \text{Eq. 1}$$

where ρ_f is the fluid density, c_f is the specific heat of the fluid, T is the temperature, t is time, $\boldsymbol{u}$ is the fluid velocity vector, and k_f is the thermal conductivity of the fluid. Application of the divergence theorem to Eq. 1 gives

$$\frac{\partial}{\partial t}\int_V \rho_f c_f T dV + \int_{\partial V} \rho_f c_f (\boldsymbol{u}\cdot\mathbf{n}) dA = \int_{\partial V} k_f (\nabla T\cdot\mathbf{n}) dA + \int_V \eta dV \quad \text{Eq. 2}$$

where V is volume, A is area and $\mathbf{n}$ is the unit normal vector. The physical meaning of each of the terms in Eq. 2 can be explained as:

- $\frac{\partial}{\partial t}\int_V \rho_f c_f T dV$ is the time derivative of the energy of the fluid cell ($= 0$ at a steady state)
- $\int_{\partial V} \rho_f c_f (\boldsymbol{u}\cdot\mathbf{n}) dA$ represents fluid advection
- $\int_{\partial V} k_f (\nabla T\cdot\mathbf{n}) dA$ represents fluid conduction
- $\int_V \eta dV$ represents particle-fluid heat transfer.

In the context of fluid flow through an assembly of particles, each of these heat transfer mechanisms is schematically illustrated in Figure 1.

This contribution focusses on developing an approach to calculate particle-fluid heat transfer ($\int_V \eta dV$ and denoted H herein) for implementation in a PNM suitable for coupling with a DEM code. The paper initially introduces the concept of using the Nusselt number to characterize particle-fluid heat transfer, then the implementation within a PNM of a Nusselt number formulation previously developed for non-circular pipes is considered. Finite volume method simulations of coupled flow and heat transfer in regular (lattice) and random (disordered) assemblies of spheres are conducted to develop and validate the novel Nusselt number formulation. The method is shown to present a viable approach to simulate particle-fluid heat transfer in particulate systems.

Application of Nusselt number to model heat flux

The Nusselt number is the ratio of convective to conductive heat transfer across a boundary. Following Caulk et al. (2020), the Nusselt number associated with a characteristic length, $\mathcal{L}$, can be defined as

$$Nu_{\mathcal{L}} = \frac{h\mathcal{L}}{k_f} \qquad \text{Eq. 3}$$

where the heat transport coefficient, h, $[\mathrm{W}/(m^2K)\ ]$ is the mean heat flux from the solid surface divided by a temperature driving force, ϑ, which is defined below (Eq. 8 and Eq. 9). If $Nu_{\mathcal{L}}$, $\mathcal{L}$ and ϑ are known, h can be determined. In a PNM the pore space is idealized as nodes, representing individual voids, connected by edges representing the connecting pore throats. In existing DEM-CFD (computational fluid dynamics) frameworks (Shimizu, 2006; Kloss et al., 2012b; Caulk et al., 2020) empirical expressions based upon either experimental or numerically-generated data were used to determine the Nusselt number. However, the PNM framework is similar to a pipe network model, and here we use the analogy between the edges in the PNM and a pipe to develop an expression for $Nu_{\mathcal{L}}$ for individual pore throats.

As illustrated in Figure 2(a), in the case of laminar flow, when fluid flow enters a pipe it is initially hydrodynamically developing, i.e. there a distance in the flow direction along which the velocity profile evolves (e.g. Shah and London, 1978). At a distance from the pipe entrance of $L = L^h$ the flow profile stabilizes and no longer evolves with distance along the

pipe, i.e. it becomes hydrodynamically fully developed. A non-dimensional hydrodynamic length, L^+ (Shah and London, 1978; Muzychka and Yovanovich, 2002) can be defined as:

$$L^+ = \frac{L}{Re\mathcal{L}} \quad \text{Eq. 4}$$

where the characteristic length, $\mathcal{L}$, reflects the pipe cross-sectional geometry and $Re = \rho_f u_f L/\mu_f$ is the Reynolds number of the flow, which depends on the density of the fluid, ρ_f, its velocity, u_f and its dynamic viscosity, μ_f. Referring to Figure 2(b), the concept of hydrodynamically developing / developed flow can be extended to consider temperature. For the case of cold fluid flow entering a pipe with a constant temperature, illustrated in Figure 2(b), at the pipe entrance there is a thermal boundary layer where the hot pipe wall influences the temperature of the flowing fluid. The thermal boundary layer grows with increasing distance from the pipe entrance; then, at a distance $L = L^t$ from the pipe entrance, the heat transport coefficient and hence also the Nusselt number become constant, and the flow becomes thermally fully developed. Following Eq. 3 , a non-dimensional thermal length (L^*) can be defined as Shah and London (1978) and Muzychka and Yovanovich (2002):

$$L^* = \frac{L}{PrRe\mathcal{L}} = \frac{L}{Pe\mathcal{L}} \quad \text{Eq. 5}$$

where Pe is the non-dimensional Peclet number, $Pe = PrRe$ which can be used to characterize heat transfer mechanisms in a fluid. The Prandtl number, Pr, depends upon the fluid properties:

$$Pr = \frac{c_f \mu_f}{k_f} \quad \text{Eq. 6}$$

According to Muzychka (1999), $L^+ \approx L^* \approx 0.05$ for the fully developed cases, calculated using L^h and L^t, respectively. Following Shah and London (1978) and Muzychka and Yovanovich (2002) we can classify a flow to be in one of the following states:

1. Hydrodynamically and thermally fully developed flow (denoted here as FD flow)
2. Hydrodynamically fully-developed but thermally developing flow, sometimes termed Graetz flow, e.g. Bennett (2019a) (denoted GZ flow herein). This is associated with $Pr > 1$.
3. Flow that is simultaneously hydrodynamically and thermally developing (SD flow)

It is impossible to have a flow that is thermally fully developed and hydrodynamically developing. In this study we restricted consideration to the case of a constant wall temperature boundary condition and FD and GZ flow conditions.

For flowing fluid it is useful to describe the temperature in terms of a "mixing cup temperature" (Whitaker, 1972). The mixing cup temperature at a cross section A is given as:

$$T_{f,A} = \frac{\int_A c_f \mu_f T(\boldsymbol{u} \cdot \boldsymbol{n}) dA}{\int_A c_f \mu_f (\boldsymbol{u} \cdot \boldsymbol{n}) dA} \qquad \text{Eq. 7}$$

Romkes et al. (2003) and Yang et al. (2010) , who also investigated particle-fluid heat transfer, considered the mean temperature difference (MTD) to determine the temperature driving force, calculated using $T_{f,A}$ at the inlet and outlet cross sections, A_{in} and A_{out}, and $T_{f,in}$ and $T_{f,out}$, respectively:

$$\vartheta_{MTD} = T_s - \frac{T_{f,in} + T_{f,out}}{2} \qquad \text{Eq. 8}$$

where T_s (constant) is the temperature of the pipe wall. However, in reality, $T_{f,A}$ varies in a non-linear manner along the pipe in the direction of flow (as illustrated in Figure 3). Previous studies including Whitaker (1972) employed a driving force expression using the logarithmic mean temperature difference ($LMTD$), which is analytically derived considering the non-linearity in $T_{f,A}$:

$$\vartheta_{LMTD} = \frac{\Delta T_{in} - \Delta T_{out}}{ln(\Delta T_{in}) - ln(\Delta T_{out})} \quad \text{Eq. 9}$$

where $\Delta\mathrm{T(L)} = \mathrm{T_s} - \mathrm{T_f(L)}$, $\mathrm{T_f(L)}$ is the mixing cup temperature at position L, and ΔT_{in} and ΔT_{out} are calculated at the pipe inlet and outlet, respectively. $LMTD$ is derived by neglecting the fluid conduction in the flow direction; thus, the accuracy of $LMTD$ decreases as the effect of conduction becomes non-negligible (i.e. a lower Pc value). Figure 4 compares the values of ϑ calculated as ϑ_{MTD} and ϑ_{LMTD} from Eq. 8 and Eq. 9, showing that $\vartheta_{MTD} \approx \vartheta_{LMTD}$ when $T_{f,in} = T_{f,out}$, but that the difference increases with increasing value of $T_{f,out} - T_{f,in}$.

Models proposed in the literature to calculate the Nusselt number (Nu) in the case of pipe flow are typically based on asymptotic analysis. In the case of FD flow the Nusselt number is constant (Shah and London, 1978), i.e. $Nu_{FD} = const$. For GZ flow, as $L^* \to 0$ the Leveque limit (Lévêque, 1928) solution is obtained (e.g. Shah and London, 1978) and for this case the asymptotic Nusselt number can be expressed as

$$Nu_{LV} \propto \left(\frac{fRe}{L^*}\right)^{1/3} \quad \text{Eq. 10}$$

Where f is the friction factor defined as

$$f = \frac{\bar{\tau}}{\frac{1}{2}\rho_f \bar{u}^2} \quad \text{Eq. 11}$$

where $\bar{\tau}$ is the mean shear stress on the pipe wall in the flow direction and $\bar{u}$ is the mean flow velocity at a representative cross section.

Muzychka and Yovanovich (2004) proposed a generalized formulation for Nu to encompass FD, LV (i.e. GZ flow at the Leveque limit), and SD conditions:

$$Nu = \left[(Nu_{FD}^{n} + Nu_{LV}^{n})^{m/n} + Nu_{SD}^{m}\right]^{1/m} \quad \text{Eq. 12}$$

Where m and n are empirical parameters obtained by fitting to experimental data. Here we neglect the Nu_{SD}, term as we exclude SD flow from the current study.

The geometry of the pore throats in a granular packing is very complex and so reference must be made to studies that considered fluid flow in non-circular pipes. The Nu_{FD} expressions developed by Yilmaz and Cihan (1993) and Bennett (2019b) for non-circular pipes are rather complex and not well suited for implementation in a PNM framework. The expression proposed by Muzychka and Yovanovich (2004) considers fRe which can be determined from the data used to develop a PNM. Here we adopt a simplified version of the Muzychka and Yovanovich expression, neglecting the term that considers the aspect ratio of the pipe cross section, as it would be difficult to define this for the pore throats. The simplified expression we consider here for non-circular (NC) pipe cross sections is given as

$$Nu_{FD,NC} = 3.24\frac{fRe_{NC}}{8\sqrt{\pi}} \quad \text{Eq. 13}$$

Muzychka and Yovanovich (2004) also enables the formulation of an expression for $\overline{Nu}_{LV,NC}$, i.e. the average Nu_{LV}, which was defined using the total heat flux from the pipe wall and the temperature driving force between the inlet and the outlet to give

$$\overline{Nu}_{LV,NC} = \frac{3}{2} 0.409 \left(\frac{fRe_{NC}}{L^*}\right)^{1/3} \quad \text{Eq. 14}$$

Combining Eq. 12, Eq. 13, and Eq. 14, the general Nusselt number for FD and LV flow in a non-circular pipe is given as

$$\overline{Nu}_{NC} = \left[\left(3.24 \frac{fRe_{NC}}{8\sqrt{\pi}}\right)^5 + \left(\frac{3}{2} 0.409 \left(\frac{fRe_{NC}}{L^*}\right)^{1/3}\right)^5\right]^{1/5} \quad \text{Eq. 15}$$

The formulation described in Eq. 15 is based on fRe (which depends on the pipe shape) and L^*.

Implementation of a thermal pore network modelling framework

To create a pore network model, the pore space must be discretized into individual pores and, in the context of DEM simulations, this discretization can be achieved effectively using a weighted Delaunay triangulation (Chareyre et al., 2012; Morimoto et al., 2022b). Each tetrahedron resulting from the weighted Delaunay triangulation defines the spatial extent of a single pore and the corresponding Voronoi vertex defines the location of the node representing that pore in the PNM. In a PNM simulation mass balance is considered for each pore assuming steady laminar and incompressible flow:

$$\sum_{i=1}^{4} Q_{ab_i} = 0 \quad \text{Eq. 16}$$

where Q_{ab_i} is the volumetric flow rate (in $[m^3 s^{-1}]$) from pore a to pore b_i, and b_i are the (four) pores adjacent to pore a. Assuming flow between any two connecting pores, a and b, to be laminar Q_{ab} is related to the pore pressures (p_a and p_b, respectively) via Darcy's law:

$$Q_{ab} = g_{ab}(p_a - p_b) \quad \text{Eq. 17}$$

where g_{ab} is the hydraulic conductance (in $[m^3 Pa^{-1} s^{-1}]$) of the throat connecting pores a and b. The conductance, g_{ab}, is related to the pore throat geometry as

$$g_{ab} = \frac{\alpha \Gamma}{\mu_f L_p} \quad \text{Eq. 18}$$

where α is a geometric factor that reflects the pore shape, L_p is the pipe length, and Γ is the conductance index in $[m^4]$. Morimoto et al. (2022b) includes a review of various expressions for Γ, and these include the hydraulic radius (HR) model proposed in Chareyre et al. (2012). The HR model considers a hydraulic radius, r_h, defined as

$$r_h = \frac{\Theta_{ab}}{\gamma_{ab}} = \frac{\Theta_{ab}}{\sum_{m=1}^{3} \gamma_{ab,m}} \quad \text{Eq. 19}$$

where, referring to Figure 5, $\gamma_{ab,m}$ is the area of the surface of particle m touching throat ab and the volume of throat ab (Θ_{ab}) is the sum of the fluid volumes in the two tetrahedra defined by pore centres and the centroids of the face three particles. Chareyre et al. (2012) proposed

$$\Gamma = 4\alpha_{HR} A_f r_h^2 \quad \text{Eq. 20}$$

where A_f is the throat face area (see Figure 6) and α_{HR} is a shape factor related to the pore geometry. Chareyre et al. (2012) suggested $\alpha_{HR} = \frac{1}{8}$ following the Hagen-Poiseuille equation. Morimoto et al. (2022b) back-calculated the α_{HR} value for three types of regular packings with a variety of void ratios and showed that the α_{HR} value is not constant but decreases as the void ratio increases (Figure 7). Once the g_{ab} values of all the pore connections are determined, Eq. 16 can be established for all the pores. If the total number of the pores in the system is M, there are M unknowns (the pressure value at each pore node) for M linear equations. By solving this system of linear equations, the pore pressure values can be

obtained. Forces on particles due to fluid flow can be calculated using the pore pressure values following Chareyre et al. (2012).

Following Caulk et al. (2020), for implementation in a PNM formulation, the fluid advection term in Eq. 2 can be expressed as

$$\int_{\partial V} \rho_f c_f (\boldsymbol{u} \cdot \boldsymbol{n}) dA = \sum_{i=1}^{4} \rho_f c_f \, T_{f,ab_i} Q_{ab_i} \qquad \text{Eq. 21}$$

where T_{f,ab_i} is the temperature of the throat connecting pores a and b_i. Caulk et al. (2020) adopted a first order upwind approach (as described in Versteeg and Malalasekera (2007) and Niyogi et al. (2009)) and set T_{f,ab_i} to be equal to the temperature of the upstream pore node.

Again as outlined in Caulk et al. (2020), the fluid conduction term in Eq. 2 can be expressed as

$$\int_{\partial V} k_f (\nabla T \cdot \boldsymbol{n}) dA = \sum_{i=1}^{4} k_f \frac{T_{b_i} - T_a}{L_{ab_i}} A_{f,ab_i} \qquad \text{Eq. 22}$$

where A_{f,ab_i} is the area of the fluid phase of the face connecting pores a and b_i, as illustrated in Figure 6.

The particle-fluid heat transfer term in Eq. 2 , i.e. H_a, is the sum of the heat transfer rates between the pore a and the particles k, $k = 1,2,3,4$, that define the pore a, and it can be expressed as

$$H_a = \sum_{k=1}^{4} H_{ka}$$

Eq. 23

246

247 If the surface area of particle k that bounds pore a is given as γ_{ka}, the mean heat flux from
248 the particle surface to the pore is H_{ka}/γ_{ka}. Referring back to Eq. 3, the heat transport
249 coefficient h_{ka} can be expressed as

$$h_{ka} = \frac{H_{ka}/\gamma_{ka}}{T_{s,k} - T_{f,a}}$$

Eq. 24

250 i.e. following Caulk et al. (2020) the temperature driving force (denoted ϑ above) is taken to
251 be the difference between the solid surface temperature $T_{s,k}$ and the pore fluid temperature
252 $T_{f,a}$. If the Nusselt number describing conduction between the surface of particle k and pore
253 a, Nu_{ka}, is known, h_{ka} can be determined from Eq. 3, allowing Eq. 23 to be expressed as

$$H_a = \sum_{k=1}^{4} H_{ka} = \sum_{k=1}^{4} Nu_{ka} \frac{\gamma_{ka} k_f \left(T_{s,k} - T_{f,a}\right)}{D_k}$$

Eq. 25

254 where D_k, the diameter of particle k, is the characteristic length used to relate Nu_{ka} and h_{ka}
255 using Eq. 3. Shimizu (2006), Kloss et al. (2012a) and Caulk et al. (2020) all used the Nusselt
256 number in their CFD-DEM frameworks, adopting empirical correlations. Caulk et al. (2020)
257 calculated Nu following Tavassoli et al. (2015) as

$$Nu = (7 - 10n + 5n^2)\left(1 + 0.1Re^{1/3}Pr^{1/3}\right) + (1.33 - 2.19n + 1.15n^2)Re^{0.7}Pr^{1/3}$$

Eq. 26

where n is the porosity. Eq. 26 was developed empirically for granular packings using data generated from Immersed Boundary Method simulations by Tavassoli et al. (2015). Caulk et al. (2020) proposed using the pore porosity, the Reynolds number at the pore, and the Prandtl number at the pore. It should be noted that Tavassoli et al. (2015)'s model was not developed at the pore-scale. Here, an alternative approach is used that determines the Nusselt number for the pore by considering the flow in a pipe with a non-circular cross section as outlined above. This approach explicitly considers the PNM modelling framework and can capture heterogeneities in the flow. Given the complexity of the pore space topology, Eq. 15 cannot be directly applied to calculate Nu, without a more detailed analysis of conduction between the particle surfaces and the fluid phase.

In this study, the applications to packed granular media are concerned; thus the velocity of the solid particles is assumed to be much smaller than the fluid velocity. The effect of the particle movement on Nu may be incorporated considering the relative velocity of the particle to the fluid; however, it remains to be future work.

Analysis of particle-fluid heat transfer via fully resolved CFD simulations

The CFD simulation approach adopted in the current study was developed from the simulation approach documented in (Morimoto et al., 2022b), which considered fluid flow but did not simulate the thermal response (i.e. isothermal conditions were implicitly assumed). The simulations were carried out with OpenFOAM (Weller et al., 1998), using the body-fit mesh generation technique developed by Knight (2021). Within OpenFOAM, BuoyantSimpleFOAM, a steady-state compressible fluid solver, was employed to solve the

continuity, momentum, and energy transport equations. The first-order upwind scheme was used as the discretisation scheme for the divergence term ($\boldsymbol{u} \cdot \nabla T$) in the energy transport equation (Eq. 1) as it was difficult to obtain the convergence using a higher order scheme. Second-order discretisation schemes were used for the divergence term $\boldsymbol{u} \cdot \nabla \boldsymbol{u}$, the gradient term, and the Laplacian term. The gravity, changes in material properties of the fluid due to temperature change, and radiative heat transfer were all neglected, so that any change the fluid temperature did not affect the fluid flow behaviour.

Validation simulations

A simple cubic (SC) packing comprising 8 particles was used to validate the fully resolved CFD simulation approach (Figure 8); this configuration as well as the applied boundary conditions were chosen to enable comparison with the numerical and experimental data reported in Romkes et al. (2003). Following Yang et al. (2010), the particle diameter used was $D = 12$ mm, and the minimum distance between particle centres was 12.12 mm. At the inlet, the fluid temperature was set to be 273 K, while at the outlet the temperature gradient was set to be zero, i.e. there was no heat conduction against the boundary at the outlet. The fluid inlet velocity (u_{inlet}) was selected to control the flow Re, while the outlet pressure was set to be 0 kPa. The lateral boundaries (orthogonal to y and z axes) were periodic. Two Re values were considered, i.e. $Re = 0.7$ and $Re = 7$.

Mesh data with key cell attribute values (i.e. temperature, velocity field) were output in vtk format from OpenFOAM to enable post-processing in Paraview (Ahrens et al., 2005). As the system comprises 8 particles on a lattice, 8 layers, one for each particle, were considered. The inlet and outlet planes for each layer are indicated on Figure 8. The bulk temperatures at

the inlet and outlet of each layer were calculated using Eq. 7. Within the Paraview software the *slice* filter was applied and the *integrateVariables* function was used to calculate both the total volumetric flow rate in the $x-$direction and the total heat rate from the particle surfaces.

The validation study focussed on selecting an appropriate inlet/outlet region lengths and the mesh size. For the simulations with $Re = 0.7$, the temperature of particle 3 was set to 313 K, while the thermal boundary condition at the surfaces of the remaining particles was specified to be adiabatic, following (Romkes et al., 2003). This scenario (i.e. low Re and almost identical fluid and particle temperatures) can lead to errors in the calculation of Nu. For the simulations with $Re = 7$, the temperature of all the particles was set to be 313 K. The Nu values for each layer (Nu_{layer}) were calculated, following Romkes *et al.* (2003), using the hydraulic diameter, d_h, as:

$$Nu_{layer} = \frac{\frac{H}{D^2} d_h}{k_f \vartheta}$$

Eq. 27

where H is the magnitude of the total heat flow from the particle surfaces as indicated on Figure 8. In a monodisperse sample, the d_h can be analytically calculated using the particle diameter D and the void ratio e of the sample as $d_h = \frac{2}{3} De$. Also following Romkes et al. (2003), ϑ was calculated from Eq. 8 (i.e. using the mean temperature difference), where $T_{f,in}$ and $T_{f,out}$ were calculated using Eq. 7 at the inlet and outlet to the layers as illustrated on Figure 8. The layer friction factor, f, was calculated following (Calis et al., 2001):

$$f = \frac{\Delta p}{\frac{1}{2}\rho_f \left(\frac{u_{inlet}}{1-\phi}\right)^2 \frac{L}{d_h}} \qquad \text{Eq. 28}$$

where u_{inlet} is the inlet velocity, ϕ is the solid fraction, L is the layer thickness, Δp is the pressure drop across the layer, defined using area averaged pressures at the inlet and outlet cross-sections (p_{in} and p_{out}) according to:

$$\Delta p = p_{in} - p_{out} = \frac{\iint_{A_{in}} p dA_{in}}{\iint_{A_{in}} dA_{in}} - \frac{\iint_{A_{ouy}} p dA_{out}}{\iint_{A_{out}} dA_{out}} \qquad \text{Eq. 29}$$

Data for layer 3 are presented here as the Nu and f values were approximately constant for layers 3-7 in agreement with Romkes et al. (2003). Two values of inlet and outlet length (D and $2D$) were considered; as illustrated in Table 1 for the various permutations of inlet and outlet length then considered the Nu and f values varied by <2%.

Additional sensitivity analyses considered the effect of the mesh size on Nu and f by varying the mesh length parameter, ds_c, illustrated on Figure 9. Following Yang et al. (2010), the ratio D/ds_c was varied between 30 and 60, noting that Morimoto et al. (2022b) found $D/ds_c = 30$ sufficient to simulate laminar flow through lattice packings of uniform spheres with no consideration of heat transfer. The data on Table 2 show that the Nu and f values stabilized at D/ds_c = 50 (the differences between the data for D/ds_c = 50 and D/ds_c = 60 were <1%). As illustrated on Figure 10 for D/ds_c=50, the data are within the 95% confidence intervals for the data in Romkes et al. (2003) (shown as max and min lines on Figure 10(a)). The f values agreed with data in Calis et al. (2001) (Figure 10(b)). An additional set of simulations for a Peclet number of Pe=4,900 confirmed that the Nu became constant for $D/ds_c \geq 50$.

Development of a pore scale Nusselt number expression using fully-resolved CFD simulations of fluid flow through lattice packings

Previous studies have shown that analysis of fluid flow through regular packings of uniform spheres can provide useful insight into particle-fluid interactions (Zick and Homsy, 1982; Morimoto et al., 2022b). Here we consider flow through three lattice packings to develop an expression for Nu that can capture fluid-particle conduction in pore throats for use in pore network models. As illustrated in Figure 11, three lattice packings of uniform spheres were considered, i.e. simple cubic (SC), body centred cubic (BCC), and face centred cubic (FCC). The void ratio of each packing was varied by adjusting the particle radius as illustrated in Table 3, and it is the densest packings that are presented on Figure 11. *MeshSpherePacking* was used with D/ds_c = 50 to discretize the void space for subsequent OpenFOAM analyses as described above.

To achieve flow that was hydrodynamically fully developed the inlet fluid velocity was selected to achieve a local Reynolds number for throat ab of approximately unity, $Re_{ab} \approx 1$, with

$$Re_{ab} = \frac{\rho_f \frac{Q_{ab}}{A_{f,ab}} d_{h,ab}}{\mu_f} \qquad \text{Eq. 30}$$

where Q_{ab} the volumetric flow rate through the throat face connecting pores a and b, $A_{f,ab}$ is the area of the pore face, $d_{h,ab}$ is the hydraulic diameter of the throat. The hydraulic diameter ($d_{h,ab}$) is four times the hydraulic radius, which is the ratio of the fluid volume Θ_{ab} to the solid surface area γ_{ab} (referring to Figure 5). For all simulations the dynamic viscosity of the fluid, $\mu_f = 1 \times 10^{-3}\ [\mathrm{Pa \cdot s}]$, the density of the fluid, $\rho_f = 1000\ \left[\frac{kg}{m^3}\right]$, and $k_f = 1\ [\mathrm{W/(K \cdot m)}]$. Since $Re = 1$ in all cases, the Peclet number ($Pe = RePr$), was adjusted by

varying the heat capacity, c_f, of the fluid, recalling that $Pr = (c_f \mu_f)/k_f$. The Pr values considered were 1.5, 4.5, 15, 45, 150, 450, 1500, and 4500; these cover the range of Pr encountered in practical applications (Morimoto, 2022).

The throats illustrated in Figure 11 (b), (d), and (f) were considered in the detailed analysis. The mixing cup temperatures at the throat inlet and outlet, T_{in} and T_{out} respectively, were calculated as

$$T_{in} = \frac{\sum_{k=1}^{3} \iint_{A_{in,k}} T \boldsymbol{u}_{in} \boldsymbol{n}_{in,k} dA_{in,k}}{\sum_{k=1}^{3} \iint_{A_{in,k}} \boldsymbol{u}_{in} \boldsymbol{n}_{in,k} dA_{in,k}} \quad \text{Eq. 31}$$

and

$$T_{out} = \frac{\sum_{k=1}^{3} \iint_{A_{out,k}} T \boldsymbol{u}_{out} \boldsymbol{n}_{out,k} dA_{out,k}}{\sum_{k=1}^{3} \iint_{A_{out,k}} \boldsymbol{u}_{out} \boldsymbol{n}_{out,k} dA_{out,k}} \quad \text{Eq. 32}$$

where $\boldsymbol{u}_{in}$, $\boldsymbol{n}_{in,k}$, $\boldsymbol{u}_{out}$, $\boldsymbol{n}_{out,k}$ are defined in the simplified 2D schematic presented in Figure 12. The numerator and denominator terms in Eq. 31 and Eq. 32 were determined by isolating the subset of the mesh that defines the face using the *slice* and *clip* filters and then applying the *calculator* filter to calculate the inner product, followed by the *integrateVariables* filter to conduct the area integration.

A key point to consider is the calculation of the temperature driving force. Both ϑ_{MTD} (Eq. 8) and ϑ_{LMTD} (Eq. 9) were determined using the T_{in} and T_{out} values calculated from Eq. 31 and Eq. 32 and the resulting Nu values are presented in Figure 13. For $L^* > 5 \times 10^{-2}$, there are noticeable differences in the Nu values calculated using ϑ_{MTD} and ϑ_{LMTD}. Where ϑ_{LMTD} is

used to calculate Nu, Nu attains a constant value at larger L^* values, in line with observations on Nu for the FD flow in pipes, and so ϑ_{LMTD} is used in subsequent analyses.

Referring to Eq. 15, $\overline{Nu}_{NC}$ depends on fRe_{NC}. Muzychka and Yovanovich (2004) proposed use of the square root of the pipe cross-sectional area ($\sqrt{A_h}$) as a characteristic length to determine both Nu and Re, however the cross-section of a pore throat is not constant, complicating the definition of a representative cross-sectional area. However, it is possible to consider the hydraulic diameter, d_h. In a pipe with a circular cross-section $d_h = d$ and so $\sqrt{A_h} = \frac{\sqrt{\pi}}{2} d_h$, and so Eq. 15 can be expressed as

$$\overline{Nu}_{d_h} = \frac{2}{\sqrt{\pi}} \left[\left(3.24 \frac{fRe_{d_h}}{16} \right)^5 + \left(\frac{3}{2} 0.393 \left(\frac{fRe_{d_h}}{L^*} \right)^{1/3} \right)^5 \right]^{1/5} \quad \text{Eq. 33}$$

fRe_{d_h} can be related to the shape factor α_{HR} in Eq. 20 ($\alpha_{HR} = 2/fRe_{d_h}$) as shown in the Appendix to this paper. Now we have

$$\overline{Nu}_{d_h} = \frac{2}{\sqrt{\pi}} \left[\left(\frac{3.24}{8\alpha_{HR}} \right)^5 + \left(\frac{3}{2} 0.393 \left(\frac{2}{\alpha_{HR} L^*} \right)^{1/3} \right)^5 \right]^{1/5} \quad \text{Eq. 34}$$

Eq. 34 shows that $\overline{Nu}_{d_h}$ depends on α_{HR} and L^*, and indicates that pipes with a similar α_{HR} should have a similar relationship between $\overline{Nu}_{d_h}$ and L^*.

Morimoto et al. (2022b) used the data in Zick and Homsy (1982) to back-calculate α_{HR} for the densest lattice packings and obtained $\alpha_{HR,FCC} = 0.1308$, $\alpha_{HR,BCC} = 0.1246$, $\alpha_{HR,SC} = 0.1277$, for the densest FCC, BCC, and SC packings respectively, while, from the Hagen

403 Pouseille equation $\alpha_{HR} = 0.125$. Figure 14(a) gives the variation in $\overline{Nu_{d_h}}$ with L^* for these
404 three dense lattice packings, and for a circular pipe; the circular pipe data are taken from Shah
405 and London (1978) while the data from the lattice packings are determined from the
406 OpenFOAM simulations. The data on Figure 14(a) show that $\overline{Nu_{d_h}}$ has a high values for low
407 values of L^* and that $\overline{Nu_{d_h}}$ attains a constant value at high values of L^*. The data on Figure
408 14(a) confirm that the $\overline{Nu_{d_h}}$ - L^* relations for these configurations with similar α_{HR} are indeed
409 similar. In all cases, the values of $\overline{Nu_{d_h}}$ are proportional to $(L^*)^{-1/3}$ in the entrance region
410 (small L^* values), confirming the applicability of the model proposed in Muzychka and
411 Yovanovich(2004) to the edges / throats in a PNM.
412
413 Figure 14(b) compares the $\overline{Nu_{d_h}}$ - L^* relationships for the three different lattice packings at
414 similar void ratios. Despite the similarity in the values of *e* there are clear differences in the
415 $\overline{Nu_{d_h}}$ that are not captured in the existing expressions for the Nusselt number in a granular
416 packing that are presented in previous studies (Ranz and Marshall, 1952; Whitaker, 1972;
417 Gunn, 1978; Li and Mason, 2000; Tavassoli et al., 2015).
418
419 The data on Figure 13 show that BCC packings with different values of e, have different Nu
420 values at a given L^*. Eq. 34 indicates that $\alpha_{HR}\overline{Nu_{d_h}}$ becomes constant as $L^* \to \infty$ and that
421 $\alpha_{HR}^{1/3}\overline{Nu_{d_h}} \propto L^{*-1/3}$ for $L^* \to 0$. Figure 15(a) plots the product $\alpha_{HR}\overline{Nu_{d_h}}$ against L^* for three
422 different values of *e* where α_{HR} is determined from analysis of the data in Zick and Homsy
423 (1982) as outlined in Morimoto et al. (2022b) (Figure 7). Comparing Figure 15(a) and Figure
424 13 it is clear that when the variation in the product $\alpha_{HR}\overline{Nu_{d_h}}$ with L^* is considered in lieu of
425 $\overline{Nu_{d_h}}$ alone, the data for the three different packing densities are unified, particularly at

higher L^* values. The correlation is further improved by considering the variation in $\alpha_{HR}^{1/3}\overline{Nu_{d_h}}$ with L^* as in Figure 15(b).

Figure 16 compares the Nu_{d_h} values obtained from the OpenFOAM simulations of the lattice packings with the Nu values predicted using the model in Muzychka and Yovanovich (2004) (denoted Nu_{MYd_h}). Linear regression of the data in Figure 16 gives $Nu_{d_h} = 1.453Nu_{MYd_h}$ with $R^2 = 0.965$. These data support use of the of the following expression to determine the Nusselt number for a throat in a PNM:

$$\overline{Nu}_{d_h} = 1.453\frac{2}{\sqrt{\pi}}\left[\left(\frac{3.24}{8\alpha_{HR}}\right)^5 + \left(\frac{3}{2}0.393\left(\frac{2}{\alpha_{HR}L^*}\right)^{1/3}\right)^5\right]^{1/5} \quad \text{Eq. 35}$$

where, following Morimoto et al. (2022b),

$$\alpha_{HR} = \frac{r_{eff}^2}{r_{eq}^2}\alpha_{ERHR} \quad \text{Eq. 36}$$

$$= \frac{r_{eff}^2}{r_{eq}^2}\left(0.510\left(\frac{1}{1+e^*}\right)^3 - 0.441\left(\frac{1}{1+e^*}\right)^2 + 286\left(\frac{1}{1+e^*}\right)\right)$$

In the expression above, r_{eq} is the equivalent radius, r_{eff} is the effective radius, and e^* is the void ratio of the throat. r_{eq} is defined as $r_{eq} = \sqrt{A_f/\pi}$ and r_{eff} is the average of the equivalent radius and the inscribed circle radius (r_{ic}) (Bryant and Blunt, 1992). As r_{eff}, r_{eq}, and e^* can be determined from the throat geometry, 1.453 is the only new empirical factor coming from the OpenFOAM simulation data. The remaining terms are based upon well-established experimental data for circular and non-circular pipes (Shah and London, 1978;

443 Y.S. Muzychka and Yovanovich, 2002; Muzychka and Yovanovich, 2004). As L^* is a function of
444 Re (Eq. 5), Eq. 35 incorporates the effects of fluid flow.
445
446 *Applicability of new expression to random assemblies of spheres*
447 To test the more general applicability of Eq. 35, flow through an assembly of random spheres
448 was considered. Following Knight (2018), an assembly of spheres with a low degree of
449 polydispersity (coefficient of uniformity, $C_u = 1.01$) was created. Three void ratio values
450 were considered, i.e. $e = 0.536, 0.610, 0.763$. As was the case for the lattice packings
451 considered above, *MeshSpherePacking* (Knight, 2021) was used to create the unstructured
452 meshes for OpenFOAM analyses. As the number of particles was larger than those had been
453 used in the lattice packing simulations the mesh resolution was slightly lower, with D/ds_c =
454 30. The analyses on the regular packings, summarized in Table 2, indicate that at this mesh
455 resolution the Nu values may be over predicted by 3-8%. The cases considered were (i) $Pe =$
456 15, $Re = 0.1$, and $Pr = 150$ and (ii) $Pe = 150$, $Re = 0.1$, and $Pr = 1500$ for all three
457 densities. Additionally, (i) $Pe = 45$, $Re = 0.1$, and $Pr = 450$ and (ii) $Pe = 1500$, $Re = 0.1$,
458 and $Pr = 15000$ were considered for the densest packing (e = 0.536).
459
460 To identify the individual pore throats the domain was discretized into pores using a modified
461 Delaunay triangulation following Chareyre et al. (2012). Throats where the edge orientation
462 and the flow field differed by more than $\pi/4$ were excluded from analysis as the PNM cannot
463 accurately capture the flow in these cases (Morimoto et al., 2022b). 30.0%, 26.6%, and 24.9%
464 of throats were excluded from analysis for e = 0.763, 0.610, and 0.536, respectively. Removing
465 such large percentages of throats from the overall analysis is not idea, and developing an
466 effective way to consider these pores should be a key focus of future work. In addition, throats

with $\vartheta < 1 \times 10^{-3}$ were excluded as the Nu values for these cases were susceptible to precision errors.

Figure 17 compares the Nu values predicted using Eq. 35 with the OpenFOAM generated data for the case with a global $Pe = 150$. Each data point represents an OpenFOAM simulation result using a regular packing with a given void ratio and Prandtl number. Data for individual throats are presented in Figure 17 and the data points are coloured based on the ratio of the throat length to the particle diameter. The fact that the data points are generally located around the line of equality supports the application of Eq. 35. Two key observations can be made for the data on Figure 17. Firstly, the Nu of the short throats with a $\frac{L_{ab}}{D} = 0.1 - 0.2$ (light blue datapoints in the graphs) tends to be lower than the predicted value; the $\frac{L_{ab}}{D}$ value for the regular packing tends to be larger (0.41-1.11) (see Table 3) and may not always represent the configurations in more realistic materials. The accurate prediction of the Nu value for such short throats remains to be future work. There is considerable scatter in the data for $5 < Nu < 10$; these low N values reflect large L^* values which may be associated with a low Re number, and thus a low fluid velocity. In these cases, the heat transfer via thermal conduction through the fluid is non-negligible compared with heat transfer via advection. The LMTD model then becomes less reliable, which is expected since thermal conduction in the fluid was not considered in its derivation. It should be noted that existing models predicting the Nusselt number were also derived neglecting fluid conduction (e.g. Gunn, 1978); thus, this issue is not unique for the proposed model. This issue becomes more prominent in the case of a low Pe value as can be seen in the data on Figure 18 which were generated for a $Pe = 15$. However, for $Pe = 1500$, this issue was not observed as Figure 19

shows and a general agreement between the OpenFOAM simulation result and the developed model.

Histograms of the relative error in the Nu values are shown in Figure 20 for (global or overall) Pe = 15, 45, 150, and 1500 with $e = 0.536$. The relative error was calculated by $\frac{Nu_{predicted} - Nu_{OpenFOAM}}{Nu_{OpenFOAM}} \times 100\ [\%]$. The short throats with $\frac{L_{ab}}{D} < 0.41$ were excluded for the analysis. A normal distribution (ND) fit was fitted to the data for each of the 4 Pe values considered and the mean value μ and the standard deviation σ were calculated. The dashed lines show the 95% confidence lines, which correspond to $\mu \pm 1.96\sigma$. For each bin the number of pores with a local $Pe < 10$ is indicated by the blue shading, while the red region indicates the number of pores with a local $Pe \geq 10$. As shown in Figure 20(a), the data for the (global) Pe = 15 indicate a considerable number of throats with local $Pe < 10$ and there are many throats with a large error ($> \pm 100\%$). However, for $Pe = 45$ (Figure 20(b)), there is a smaller number of throats with (local) $Pe < 10$ and the mean value relative error was 13.17%. For $Pe = 150$ and $Pe = 1500$ (Figure 20(c) and (d)), there were negligible numbers of throats with local Pe < 15 and the μ values were close to zero. Based on the analysis shown in Figure 20, the model can be applied with reasonable accuracy for a global $Pe > 45$; however, it is recommended to restrict application of the model to scenarios where the global $Pe > 150$.

The model proposed here is limited, as in its current form it is not applicable to simultaneously developing flow. However for the dataset developed here, the model is shown to be capable of predicting the pore-scale Nusselt number values for various Graetz flow conditions especially well for global $Pe > 150$. As shown in Appendix B, we know of no other published

model that can predict the Nusselt number for Graetz flow with comparable accuracy. Adaption of this model for simultaneously developing flow may be addressed in future work. This study has been motivated by applications that consider densely packed granular media (e.g. a deposit of sand at rest); thus the velocity of the solid particles is assumed to be much smaller than the fluid velocity. The effect of the particle movement on the Nu values may be incorporated considering the relative velocity of the particle to the fluid; this may be explored in future research.

Conclusions

This study has proposed a novel particle-fluid heat transfer model for inclusion in a simulation framework that couples the Discrete Element Method (DEM) with a Pore Network Model (PNM) to simulate laminar flow through granular materials. Models predicting wall-fluid conductive heat flux (or equivalently Nusselt number) in circular and non-circular pipes were used to develop this model. This study showed that the shape factor α, commonly used to determine the edge conductances in a PNM, can be related to the product of the friction factor f and the Reynolds number Re. This correlation indicated that a previous model proposed to predict wall-fluid conduction in non-circular pipes which used fRe (Muzychka and Yovanovich, 2004) can be used to predict the particle-fluid heat transfer in PNM. In this work we developed a fully-resolved CFD dataset using regular packings and considering laminar fluid flow while applying a temperature gradient across the sample. In these CFD simulations, the Peclet number was varied and pore-scale Nu values were extracted from the CFD data to develop the new particle-fluid heat transfer model proposed here for DEM-PNM. To validate the new model, a fully-resolved CFD dataset using random packings was

developed. The local, or throat, Nu values were extracted from the CFD simulation results and compared with the predicted Nu values.

The key finding of this study is that the Nu expression for pipes can be used to describe local- or pore-scale particle-fluid heat transfer in granular materials. This has the potential to improve the accuracy of thermal DEM-PNM modelling frameworks. The following additional conclusions can be drawn from this work:

1. The results from fully-resolved CFD simulations considering flow through regular, lattice packings of uniform spheres showed that the local- or pore-scale Nusselt number (Nu) value tends to be constant for $L^* \to \infty$ and proportional to $L^{*-\frac{1}{3}}$ for $L^* \to 0$, where L^* is the non-dimensional thermal length defined in Eq. 5. Despite the complexity of the pore-space topology, and the variation in the pore geometry along a path between connected voids, this observation is in accordance with the previous experimental and analytical studies for circular and non-circular pipes with a constant cross-section.
2. The expression for the Nu value in a circular pipe developed by Muzychka and Yovanovich (2004) was shown to have a linear correlation with the Nu values obtained from the CFD simulations for the regular , lattice packings. This important observation enabled development of a new expression for the Nu value for an individual pore throat in a granular material, i.e. an edge in a PNM. The new expression was developed by adding only one empirical parameter to the Muzychka and Yovanovich (2004) model to give

$$\overline{Nu}_{d_h} = C\frac{2}{\sqrt{\pi}}\left[\left(\frac{3.24}{8\alpha_{HR}}\right)^5 + \left(\frac{3}{2}0.393\left(\frac{2}{\alpha_{HR}L^*}\right)^{1/3}\right)^5\right]^{1/5}$$

where C is an empirical parameter obtained by linear regression and determined to be 1.453 in the current study. The α_{HR} can be calculated following Morimoto et al. (2022b)'s analytical study only using the void ratio of the throat. Consequently, the expression is much simpler than any of the previous models predicting the Nusselt number in granular materials.

3. The Nu value for throats in a random assembly of spheres predicted by the developed model showed a good agreement with the Nu value obtained from the CFD simulation data. However this agreement could only be confirmed for relatively high Pe values; validation for a low Pe is not straightforward value due to the difficulty in obtaining Nu values under scenarios when heat is transferred mainly by conduction, which is typically the case for a low Pe value.
4. A thermal PNM that includes the expression developed here presents an efficient and accurate option for simulating heat transfer phenomena in granular materials with the laminar pore fluid flow. The capacity to model heat transfer in most of the throats in the random packings considered here will undoubtedly lead to improved scientific understanding of heat transfer phenomena in granular materials. However, there are several issues which need to be addressed to enable application to a broader range of pore throat topologies and Pe numbers. Specifically, improvements are needed in the case of pore throats with low Pe values, throats whose edge-orientation and flow direction differ, and short throats.

Acknowledgements

Dr. Tokio Morimoto was funded by the European Union's Horizon 2020 research and innovation program Marie Skłodowska-Curie grant agreement MATHEGRAM No. 813202.

OpenFOAM simulations were conducted on the Research Computing Service facilities at Imperial College London (DOI: 10.14469/hpc/2232).

590 **Appendix A**

591

592 Eq. 15 expresses Nu as a function of the product fRe, and fRe can, in turn, be expressed in
593 terms of α_{HR} in Eq. 20, which will be shown in this appendix. As shown in Eq. 11, f depends
594 on $\bar{\tau}$. In the case of steady flow the pressure drop in a pipe (Δp) is related to the product of
595 $\bar{\tau}$ and the surface area of the pipe, γ:

596

$$\bar{\tau}\gamma = \Delta pA \qquad \text{Eq. 37}$$

597

598 where A is the cross-sectional area. Thus, we can write

599

$$\bar{\tau} = \frac{\Delta pA}{\gamma} = \Delta p \frac{d_h}{4L} \qquad \text{Eq. 38}$$

600

601 where d_h, the hydraulic diameter is $d_h = 4\Theta/\gamma = 4AL/\gamma$. Substitution of Eq. 38 into Eq. 11
602 gives

603

$$f = \frac{\Delta p \frac{d_h}{L}}{2\rho_f \bar{u}^2} \qquad \text{Eq. 39}$$

604

605 The Reynolds number for a characteristic length $\mathcal{L}$ is

606

$$Re_{\mathcal{L}} = \frac{\rho_f \bar{u} \mathcal{L}}{\mu_f} \qquad \text{Eq. 40}$$

607

608 and

$$fRe_{\mathcal{L}}=\frac{\Delta p d_h \mathcal{L}}{2\mu_f L\bar{u}} \quad \text{Eq. 41}$$

609

610 Now $\bar{u} = Q/A$ and so we can write

611

$$Q =\frac{\mathrm{A}\Delta p d_h \mathcal{L}}{2fRe_{\mathcal{L}}\mu_f L} \quad \text{Eq. 42}$$

612

613 or, if d_h is the characteristic length:

614

615

$$Q =\frac{1}{2fRe_{d_h}}\frac{\mathrm{A}d_h^2}{\mu_f L}\Delta p = \frac{8}{fRe_{d_h}}\frac{\mathrm{A}r_h^2}{\mu_f L}\Delta p \quad \text{Eq. 43}$$

616

617 Referring back to equations Eq. 17, Eq. 18, and Eq. 19, we can say

618

$$\alpha_{HR} = \frac{2}{fRe_{d_h}} \quad \text{Eq. 44}$$

619

620

621

622 **Appendix B**

623 Hitherto various equations predicting Nu in packed granular bed have been proposed and
624 used in coupled CFD-DEM simulations. Whitaker (1972) proposed the following expression
625 for Nu:

626

$$Nu = \left(0.5Re^{\frac{1}{2}} + 0.2Re^{\frac{2}{3}}\right)Pr^{\frac{1}{3}} \qquad \text{Eq. 45}$$

627

628 which is used in a CFD-DEM proposed by Shimizu et al. (2006). Caulk et al. (2019) proposed
629 use of the expression in Tavassoli et al. (2015) given as:

630

$$Nu = (7 - 10n + 5n^2)\left(1 + 0.1Re^{\frac{1}{5}}\mathrm{Pr}^{\frac{1}{3}}\right) + (1.33 - 2.19n + 1.15n^2)Re^{0.7}Pr^{\frac{1}{3}} \qquad \text{Eq. B.2}$$

631

632 Eq. B.2 is a modified version of the following expression proposed in Gunn (1978):

$$Nu = (7 - 10n + 5n^2)\left(1 + 0.7Re^{\frac{1}{5}}\mathrm{Pr}^{\frac{1}{3}}\right) + (1.33 - 2.4n + 1.2n^2)Re^{0.7}Pr^{\frac{1}{3}} \qquad \text{Eq. B.3}$$

633 Equations B.1 to B.3 were developed empirically from experimental or numerical simulation
634 data.

635

636 Equations B.1 to B.3 were developed empirically from experimental or numerical simulation
637 data. Table B.1 gives the Nu values predicted by these three expressions for porosities
638 between 0.3 and 0.7 and $Re = 0.1$ and $Pr = 1500$.

639

640 Referring to Table B.1, there is no agreement among these three models. Figure B.1
641 compares the Nu values obtained from the numerical simulations conducted in this study
642 and the Nu values predicted by Equations B.1 to B.3. None of these expressions cannot
643 predict the Nu values observed in the simulatioins as accurately as the model proposed in
644 this study. The main reason for the poor agreement between the simulation data and the
645 existing models os that Equations B.1 – B.3 were developed for simultaneously developing
646 flow but the simulation data consider Graetz flow (hydro-dyncamically fully-redeveloped
647 but thermally-developing flow). However. the new model proposed in this contribution
648 model cannot predict the Nu value for simultaneously-developed flow. These data highlight
649 the need to consider the nature of the flow when selecting an approach to predict Nu
650 values.
651

652

653 **References**

654

655 Ahrens, J., Geveci, B. and Law, C. (2005) *ParaView: An End-User Tool for Large Data*
656 *Visualization,*. Elsevier,.

657 Bennett, T. D. (2019a) 'Correlations for the Graetz problem in convection – Part 1: For round
658 pipes and parallel plates', *International Journal of Heat and Mass Transfer*, 136, pp. 832–
659 841. doi: 10.1016/j.ijheatmasstransfer.2019.03.006.

660 Bennett, T. D. (2019b) 'Correlations for the Graetz problem in convection – Part 2: For ducts
661 of arbitrary cross-section', *International Journal of Heat and Mass Transfer*, 135, pp. 1327–
662 1334. doi: 10.1016/j.ijheatmasstransfer.2019.02.052.

663 Bryant, S. and Blunt, M. (1992) 'Prediction of relative permeability in simple porous media',
664 *Physical Review A*, 46(4), pp. 2004–2011. doi: 10.1103/PhysRevA.46.2004.

665 Calis, H. P. A., Nijenhuis, J. P. B. C., Paikert, B. C., Dautzenberg, F. M., and Van Den Bleek, C.
666 M. (2001) CFD modelling and experimental validation of pressure drop and flow profile in a
667 novel structured catalytic reactor packing, *Chemical Engineering Science*, 56(4), pp. 1713–
668 1720. doi: 10.1016/S0009-2509(00)00400-0.

669 Caulk, R., Scholtes, L., Krzaczek, M., & Chareyre, B. (2020) A pore-scale thermo–hydro-
670 mechanical model for particulate systems, *Computer Methods in Applied Mechanics and*
671 *Engineering*, 372, p. 113292. doi: 10.1016/j.cma.2020.113292.

672 Chareyre, B., Cortis, A., Catalano, E., & Barthélemy, E. (2012) 'Pore-Scale Modeling of
673 Viscous Flow and Induced Forces in Dense Sphere Packings', *Transport in Porous Media*,
674 94(2), pp. 595–615. doi: 10.1007/s11242-012-0057-2.

675 Feng, Y. T., Han, K. and Owen, D. R. J. (2009) 'Discrete thermal element modelling of heat

676 conduction in particle systems: Pipe-network model and transient analysis', *Powder*
677 *Technology*, 193(3), pp. 248–256. doi: 10.1016/j.powtec.2009.03.001.
678 Gunn, D. J. (1978) 'Transfer of heat or mass to particles in fixed and fluidised beds',
679 *International Journal of Heat and Mass Transfer*, 21(4), pp. 467–476. doi: 10.1016/0017-
680 9310(78)90080-7.
681 Kloss, C. *et al.* (2012) 'Models, algorithms and validation for opensource DEM and CFD-
682 DEM.', *Progress in Computational Fluid Dynamics, An International Journal*, 12(2/3), pp.
683 140–152. doi: 10.1504/PCFD.2012.047457.
684 Knight, C. S. (2018) *Fluid flow and drag in polydisperse granular materials subject to laminar*
685 *seepage flow*. Imperial College London.
686 Knight, C. S. (2021) *mesh-sphere-packing*. Available at: https://github.com/chrisk314/mesh-
687 sphere-packing.
688 Lévêque, A. M. (1928) 'Les lois de la transmission de chaleur par convection', *Annales des*
689 *Mines,* 13, pp. 201–415.
690 Li, J. & Mason, D. (2000) A computational investigation of transient heat transfer in
691 pneumatic transport of granular particles. Powder Technology. 112 (3), 273–282.
692 Morimoto, T. (2022) *Particle-scale numerical simulation of the thermal behaviour of*
693 *granular materials*. Imperial College London.
694 Morimoto, T., O'Sullivan, C. and Taborda, D. M. G. (2022a) Exploiting DEM to Link Thermal
695 Conduction and Elastic Stiffness in Granular Materials, *Journal of Engineering Mechanics*,
696 148(2). doi: 10.1061/(ASCE)EM.1943-7889.0002054.
697 Morimoto, T., Zhao, B., Taborda, D. M. G., and O'Sullivan, C. (2022b) Critical appraisal of
698 pore network models to simulate fluid flow through assemblies of spherical particles,
699 *Computers and Geotechnics*, 150, p. 104900. doi: 10.1016/j.compgeo.2022.104900.

Muzychka, Y. S. (1999) *Analytical and experimental study of fluid friction and heat transfer in low Reynolds number flow heat exchangers.* University of Waterloo.

Muzychka, Y. S. and Yovanovich, M. M. (2002) Laminar flow friction and heat transfer in non-circular ducts and channels part 1: Hydrodynamic problem., in *Compact Heat Exchangers: a festschrift on the 60th birthday of Ramesh K. Shah : proceedings of the International Symposium on Compact Heat Exchangers*. Pisa: Edizioni ETS, Pisa, pp. 123-130.

Muzychka, Y. S. and Yovanovich, M. M. (2002) Laminar Flow Friction and Heat Transfer in Non- Circular Ducts and Channels Part II: Thermal Problem. , in *Compact Heat Exchangers: a festschrift on the 60th birthday of Ramesh K. Shah : proceedings of the International Symposium on Compact Heat Exchangers*. Grenoble,: Edizioni ETS, Pisa, pp. 131-139.

Muzychka, Y. S. and Yovanovich, M. M. (2004) Laminar Forced Convection Heat Transfer in the Combined Entry Region of Non-Circular Ducts, *Journal of Heat Transfer*, 126(1), pp. 54–61. doi: 10.1115/1.1643752.

Niyogi, P., Chakrabartty, S. K. and Laha, M. K. (2009) *Introduction to Computational Fluid Dynamics*. Pearson Education.

Ranz, W & Marshall, W (1952) Evaporation from drops. Chemical Engineering Progress. 48, 141–146.

Romkes, S. J. P., Dautzenberg, F. M., Van den Bleek, C. M., and Calis, H. P. A. (2003) CFD modelling and experimental validation of particle-to-fluid mass and heat transfer in a packed bed at very low channel to particle diameter ratio, *Chemical Engineering Journal*, 96(1–3), pp. 3–13. doi: 10.1016/j.cej.2003.08.026.

Shah, R. K. and London, A. L. (1978) *Laminar Flow Forced Convection in Ducts*. Elsevier. doi: 10.1016/C2013-0-06152-X.

724 Shimizu, Y. (2006) Three-dimensional simulation using fixed coarse-grid thermal-fluid
725 scheme and conduction heat transfer scheme in distinct element method, *Powder*
726 *Technology*, 165(3), pp. 140–152. doi: 10.1016/j.powtec.2006.04.003.
727 Sufian, A. *et al.* (2019) 'Ability of a pore network model to predict fluid flow and drag in
728 saturated granular materials', *Computers and Geotechnics*, 110. doi:
729 10.1016/j.compgeo.2019.02.007.
730 Tavassoli, H., Peters, E. A. J. F. and Kuipers, J. A. M. (2015) 'Direct numerical simulation of
731 fluid–particle heat transfer in fixed random arrays of non-spherical particles', *Chemical*
732 *Engineering Science*, 129, pp. 42–48. doi: 10.1016/j.ces.2015.02.024.
733 Versteeg, H. K. and Malalasekera, W. (2007) *An introduction to computational fluid*
734 *dynamics: the finite volume method.* Pearson Education.
735 Weller, H. G., Tabor, G., Jasak, H., and Fureby, C. (1998) A tensorial approach to
736 computational continuum mechanics using object-oriented techniques, *Computers in*
737 *Physics*, 12(6), p. 620. doi: 10.1063/1.168744.
738 Whitaker, S. (1972) Forced convection heat transfer correlations for flow in pipes, past flat
739 plates, single cylinders, single spheres, and for flow in packed beds and tube bundles, *AIChE*
740 *Journal*, 18(2), pp. 361–371. doi: 10.1002/aic.690180219.
741 Yang, J., Wang, Q., Zeng, M., and Nakayama, A. (2010) Computational study of forced
742 convective heat transfer in structured packed beds with spherical or ellipsoidal particles,
743 *Chemical Engineering Science*, 65(2), pp. 726–738. doi: 10.1016/j.ces.2009.09.026.
744 Yilmaz, T. and Cihan, E. (1993) General equation for heat transfer for laminar flow in ducts
745 of arbitrary cross-sections, *International Journal of Heat and Mass Transfer*, 36(13), pp.
746 3265–3270. doi: 10.1016/0017-9310(93)90009-U.
747 Yun, T. S. and Evans, T. M. (2010) Three-dimensional random network model for thermal

conductivity in particulate materials, *Computers and Geotechnics*, 37(7–8), pp. 991–998. doi: 10.1016/j.compgeo.2010.08.007.

Yun, T. S. and Santamarina, J. C. (2008) 'Fundamental study of thermal conduction in dry soils', *Granular Matter*, 10(3), pp. 197–207. doi: 10.1007/s10035-007-0051-5.

Zick, A. A. and Homsy, G. M. (1982) 'Stokes flow through periodic arrays of spheres', *Journal of Fluid Mechanics*, 115(1), p. 13. doi: 10.1017/S0022112082000627.

Notation

Latin

A	Area
$A_{f,ab}$	Area of the fluid phase of the face connecting pores a and b
A_{in}	Pipe inlet cross section
A_{out}	Pipe outlet cross section
BCC	Body centred cubic lattice packing
c_f	Specific heat of fluid
$d_{h,ab}$	Hydraulic diameter of the throat connecting pores a and b
d_h	Hydraulic diameter
D	Particle diameter
f	Friction factor
FCC	Face centred cubic lattice packing
FD	Hydrodynamically and thermally fully developed flow
g_{ab}	Hydraulic conductance of the throat connecting pores a and b.
GZ	Hydrodynamically fully-developed but thermally developing flow(Graetz flow)
h	Heat transfer coefficient at fluid-solid boundary
H	Particle-fluid heat transfer term
HR	Hydraulic radius model for pore conductance
k_f	Thermal conductivity of fluid
L	Distance along pipe from entrance in the direction of flow

L^h	Distance from pipe entrance at which flow becomes hydrodynamically fully developed
L_p	Pipe length in a PNM
$LMTD$	Logarithmic mean temperature difference
MTD	Mean temperature difference
n	Porosity
$\mathbf{n}$	Unit normal vector
Nu	Nusselt number
Nu_{layer}	Nusselt number for a layer in the SC packing
Nu_{FD}	Nusselt number for fully developed flow
Nu_{LV}	Nusselt number calculated at the Leveque limit
p_a	Pressue in pore a
Pe	Peclet number
Q_{ab_i}	The volumetric flow rate from pore a to pore b_i
R	Pipe radius in PNM
Re	Flow Reynolds number
SC	Simple cubic packing
SD	Flow that is simultaneously hydrodynamically and thermally developing
T	temperature
$T_{f,A}$	Mixing cup temperature for cross section A
$\mathrm{T_f(L)}$	Mixing cup temperature at position L along pipe
$T_{f,in}$	Mixing cup temperature at pipe inlet
$T_{f,out}$	Mixing cup temperature at pipe outlet

$T_{f,ab}$	Temperature of the throat connecting pores a and b .
T_s	Temperature of solid particle face
t	Time
$\boldsymbol{u}$	Fluid velocity vector
$\bar{u}$	Mean flow velocity at a representative cross section
V	Volume

758

759

760 Greek

α	Geometric factor to determine conductance in a PNM
ΔT_{in}	Difference between solid face temperature and mixing cup temperature at pipe inlet
ΔT_{out}	Difference between solid face temperature and mixing cup temperature at pipe outlet
ϑ	Temperature driving force
ϑ_{LMTD}	Temperature driving force calculated using the logarithmic mean temperature difference
ϑ_{MTD}	Temperature driving force calculated using the mean temperature difference
η	Energy input to fluid per unit volume via particle-fluid convection
ϕ	Solid fraction
ρ_f	Fluid density
$\mathcal{L}$	Characteristic length

μ	Mean value in a standard distribution fit
μ_f	Dynamic viscosity of fluid
σ	Standard deviation in a standard distribution fit
$\bar{\tau}$	Mean shear stress on the pipe wall in the flow direction
γ_{ab}	Surface area of throat ab
γ_{ka}	Surface area of particle k that bounds pore a
Θ_{ab}	Fluid volume in throat ab

761

762

763

764

765

766

767

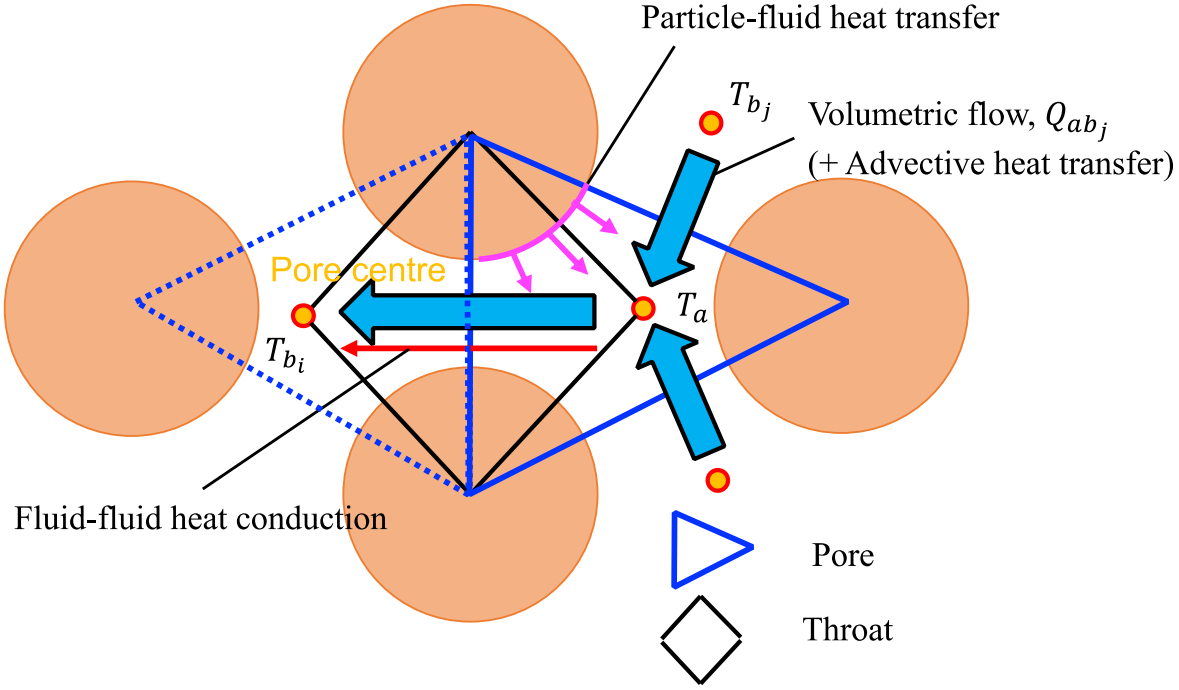
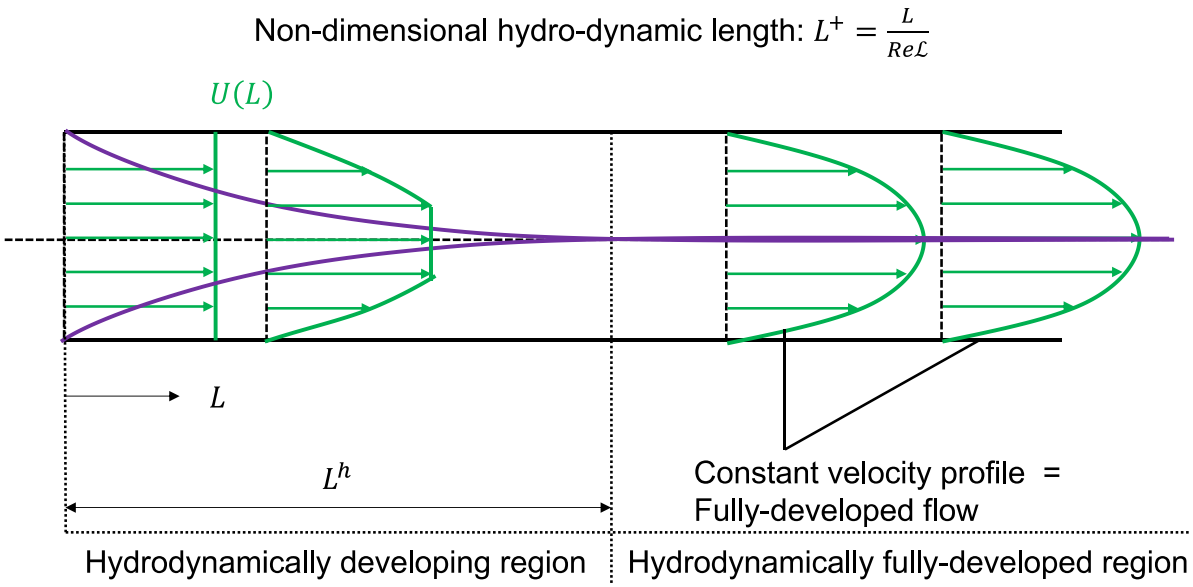
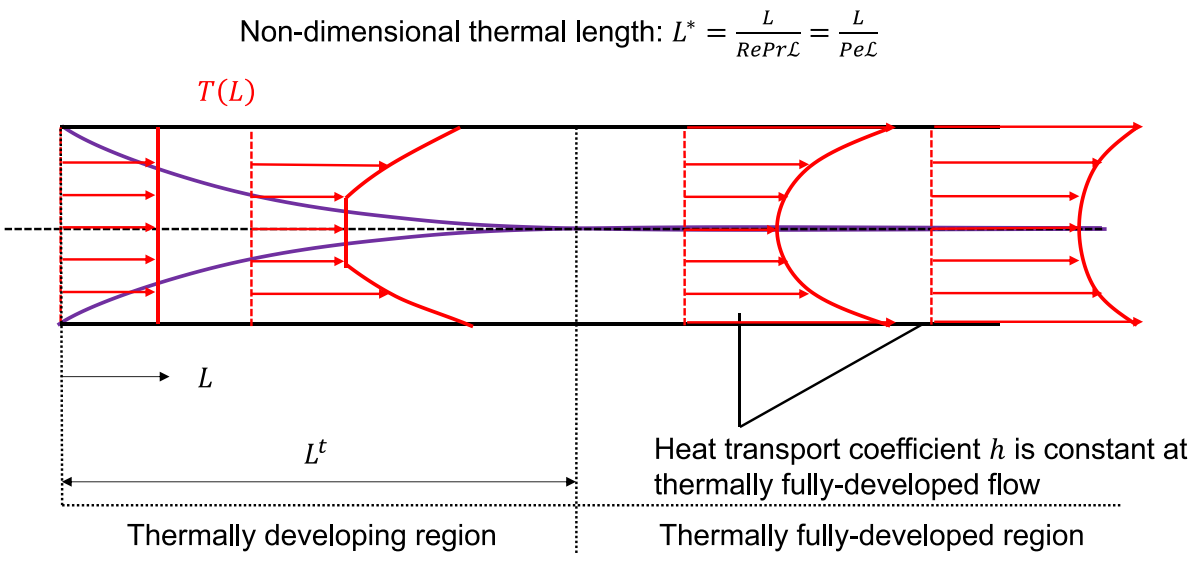


Figure 1 Schematic illustration of the thermal PNM proposed by Caulk et al. (2020) (presented in 2D for clarity)

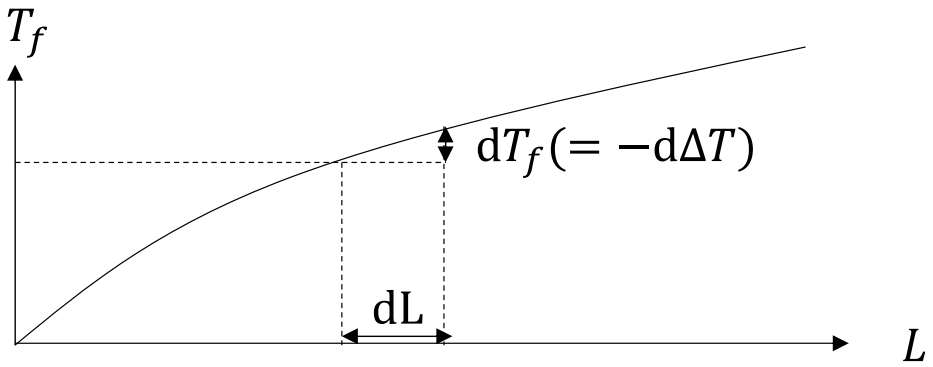


(a)



(b)

Figure 2 Schematic illustrations of (a) the development of velocity profile for laminar fluid flow in a cylindrical pipe and (b) the temperature profile in the fluid

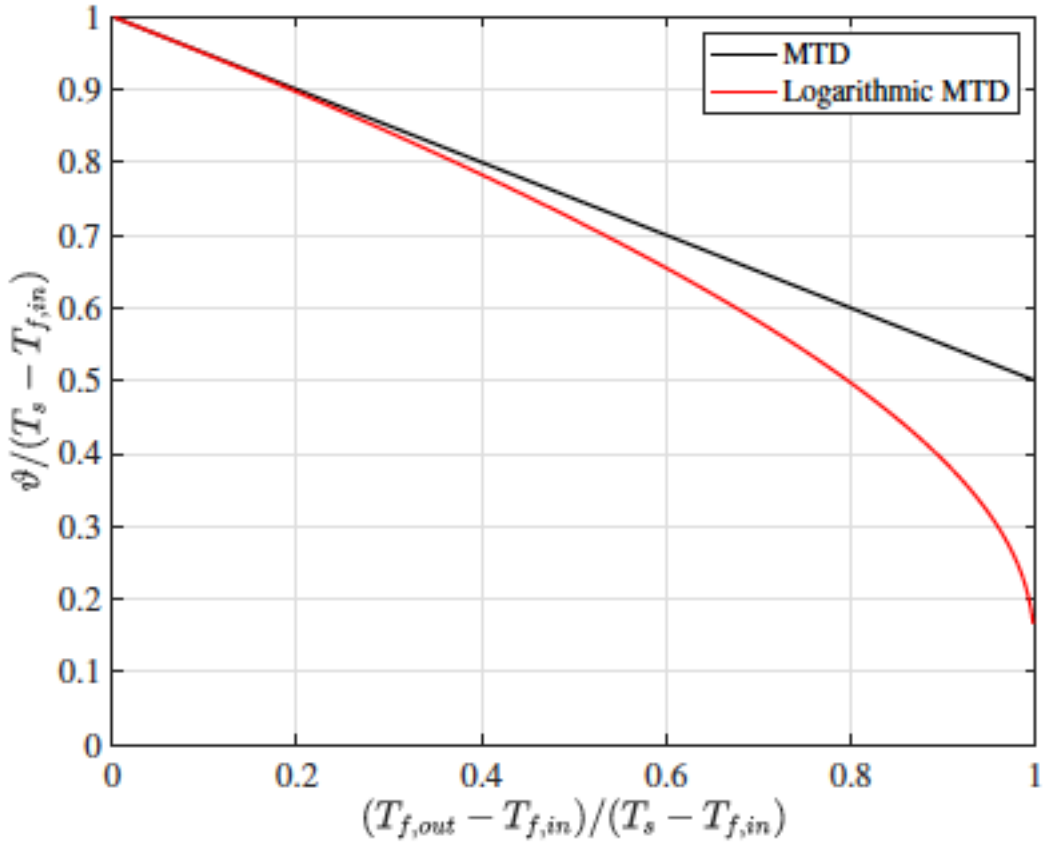


786

787 *Figure 3 Variation in fluid temperature with position along pipe: Illustration to explain calculation of*

788 *analytically-derived temperature driving force*

789



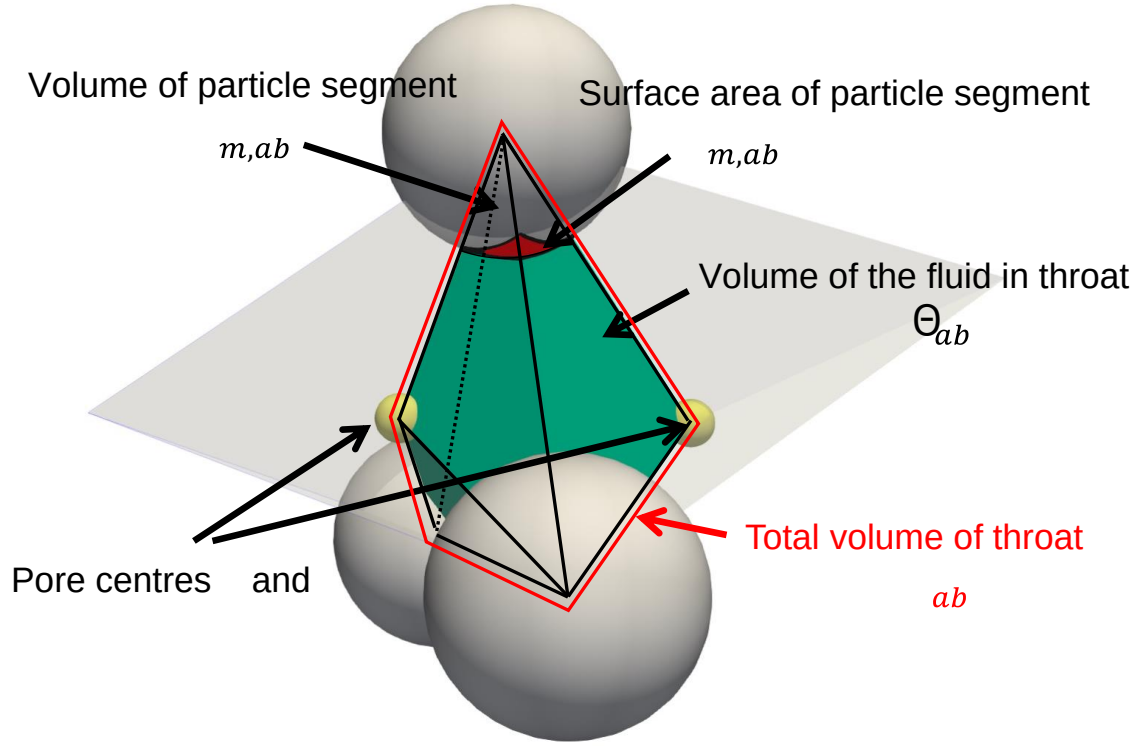
790

791

792 *Figure 4 Variation in ϑ with $T_{f,out} - T_{f,in}$: Comparison of MTD and LMTD – data are normalised by $T_s -$*

793 *T_f, in*

794

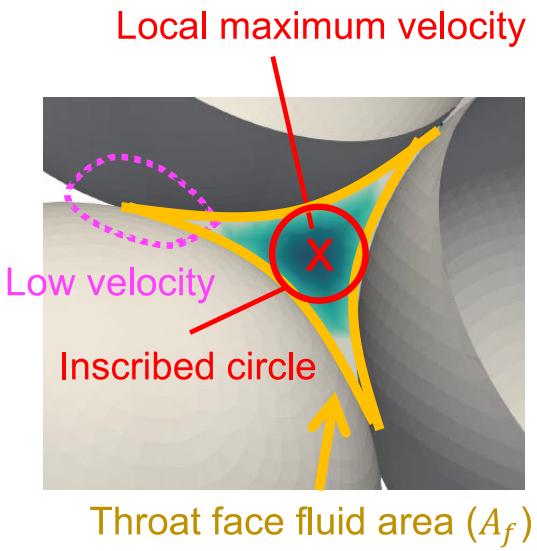


795

796

797 *Figure 5 Illustration of the total volume of a throat, the volume of fluid and the surface area.*

798



799

800

801 *Figure 6 Definition of A_f*

802

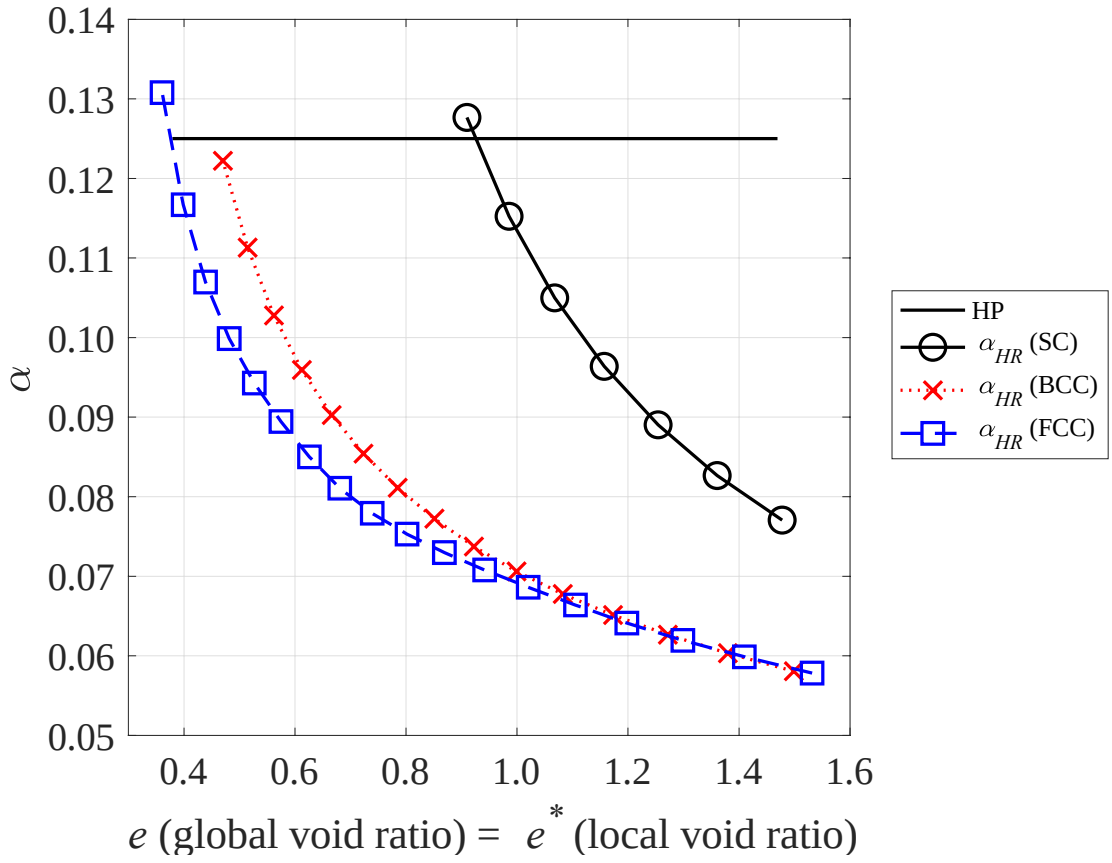


Figure 7 α_{HR} values back-calculated from Zick and Homsy (1982) by Morimoto et al. (2022b) for three types of regular packings with a wide range of void ratio values. HP stands for Hagen-Poiseuille flow ($\alpha_{HR} = 1/8$).

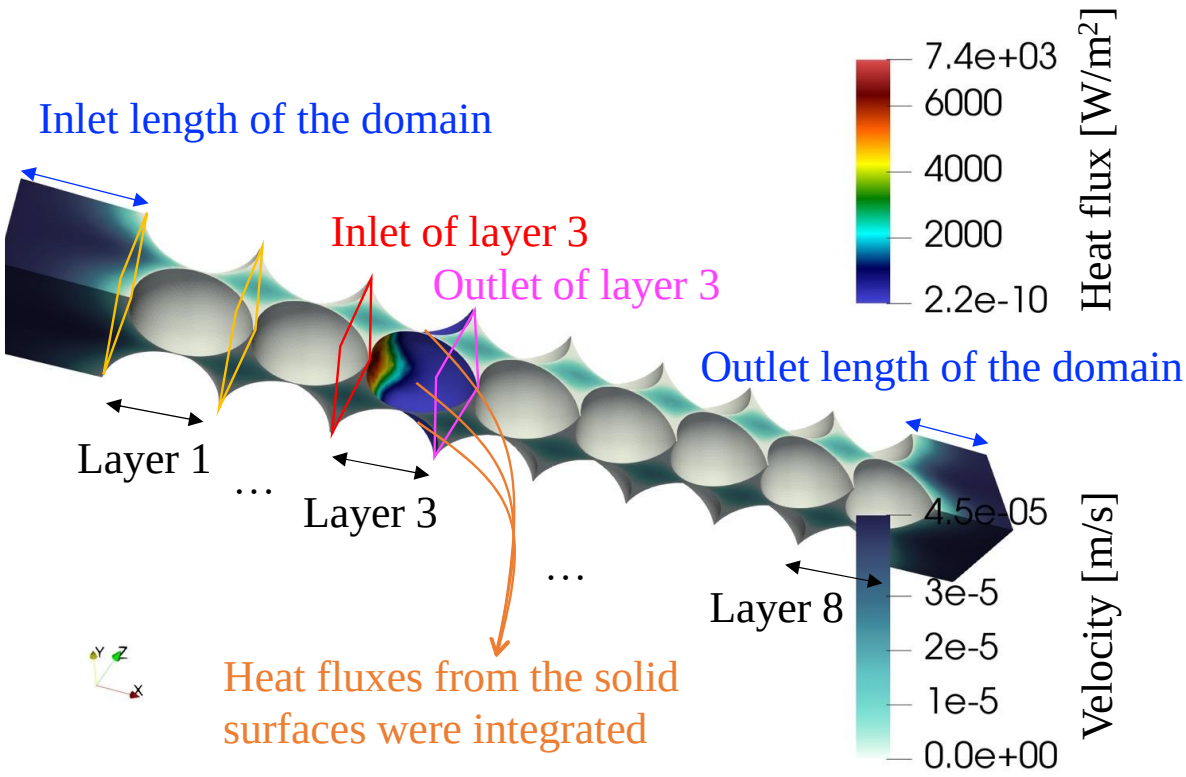


Figure 8 Validation case geometry

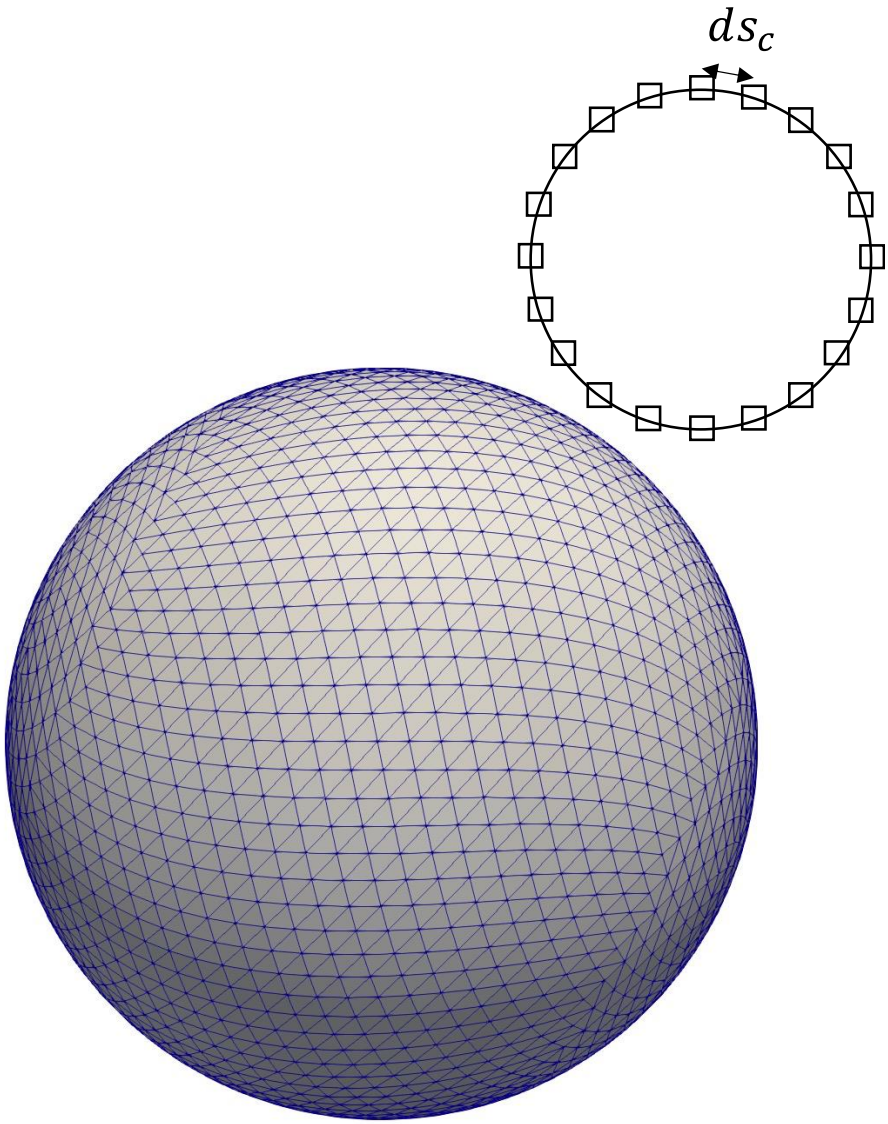
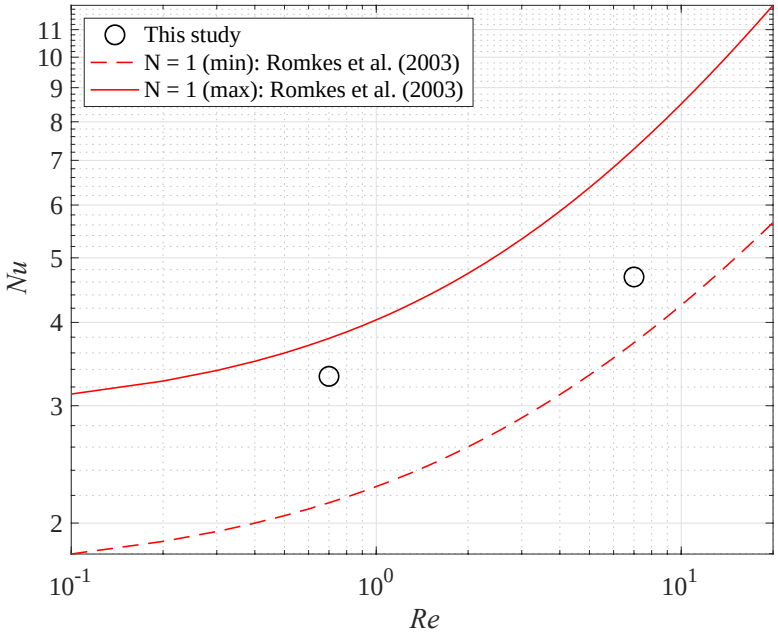
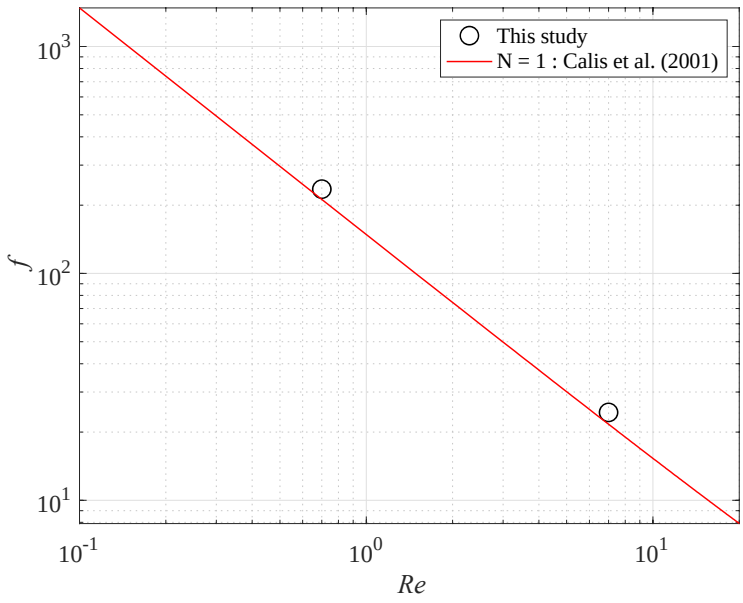


Figure 9 Schematic diagram explaining ds_c parameter used to specify mesh size.



(a)



(b)

Figure 10 Comparison of results at $D/ds_c = 50$ against previous CFD studies (Romkes et al., 2003; Calis et al., 2001). (a) Variation in Nu with Re (b) Variation in f with Re

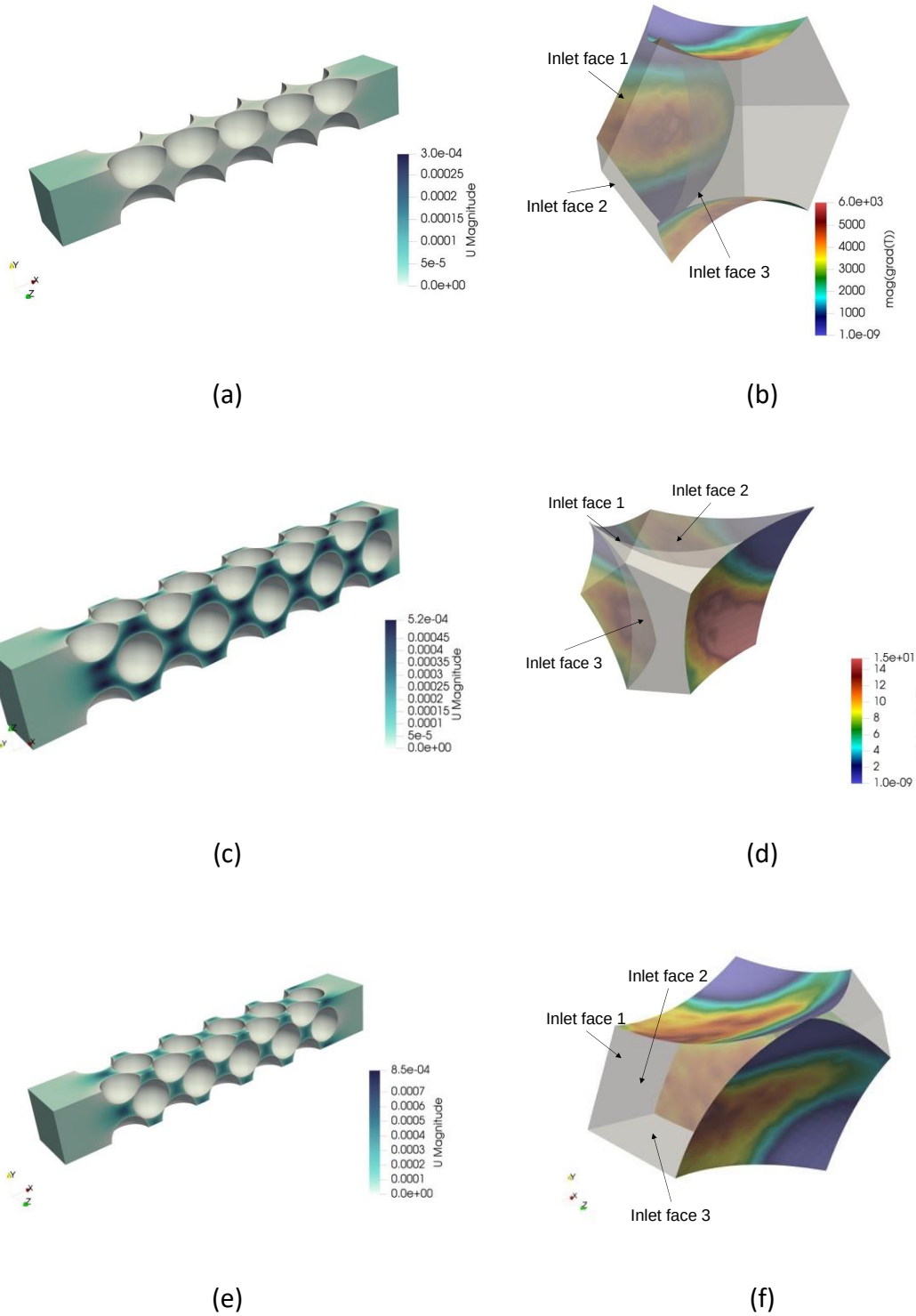
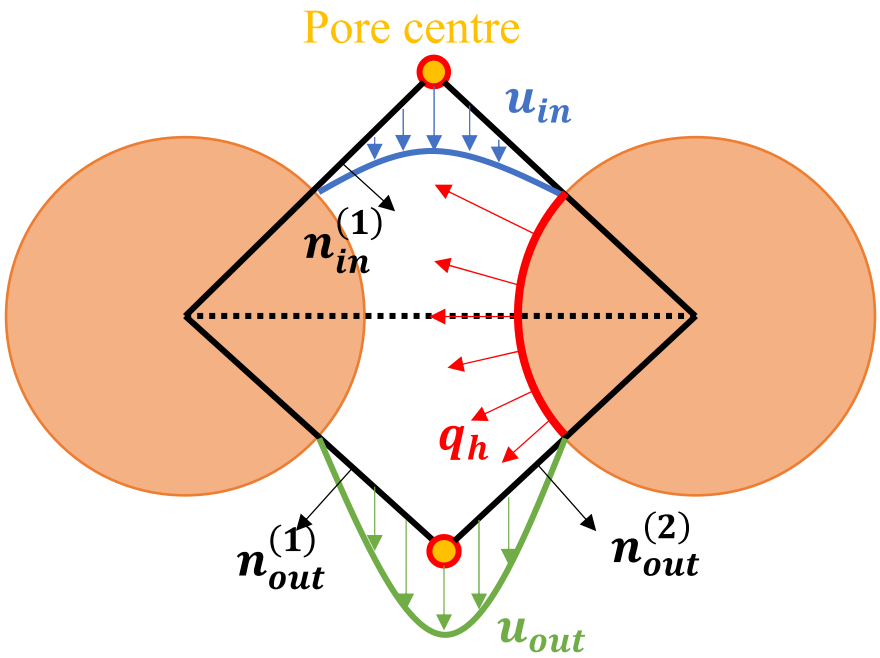


Figure 11 Geometry of regular packings. (a) SC (b) SC throat (c) BCC (d) BCC throat (e) FCC (f) FCC throat. (a), (c), and (e) are coloured based on the velocity and (b), (d), and (f) are coloured based on the heat flux.

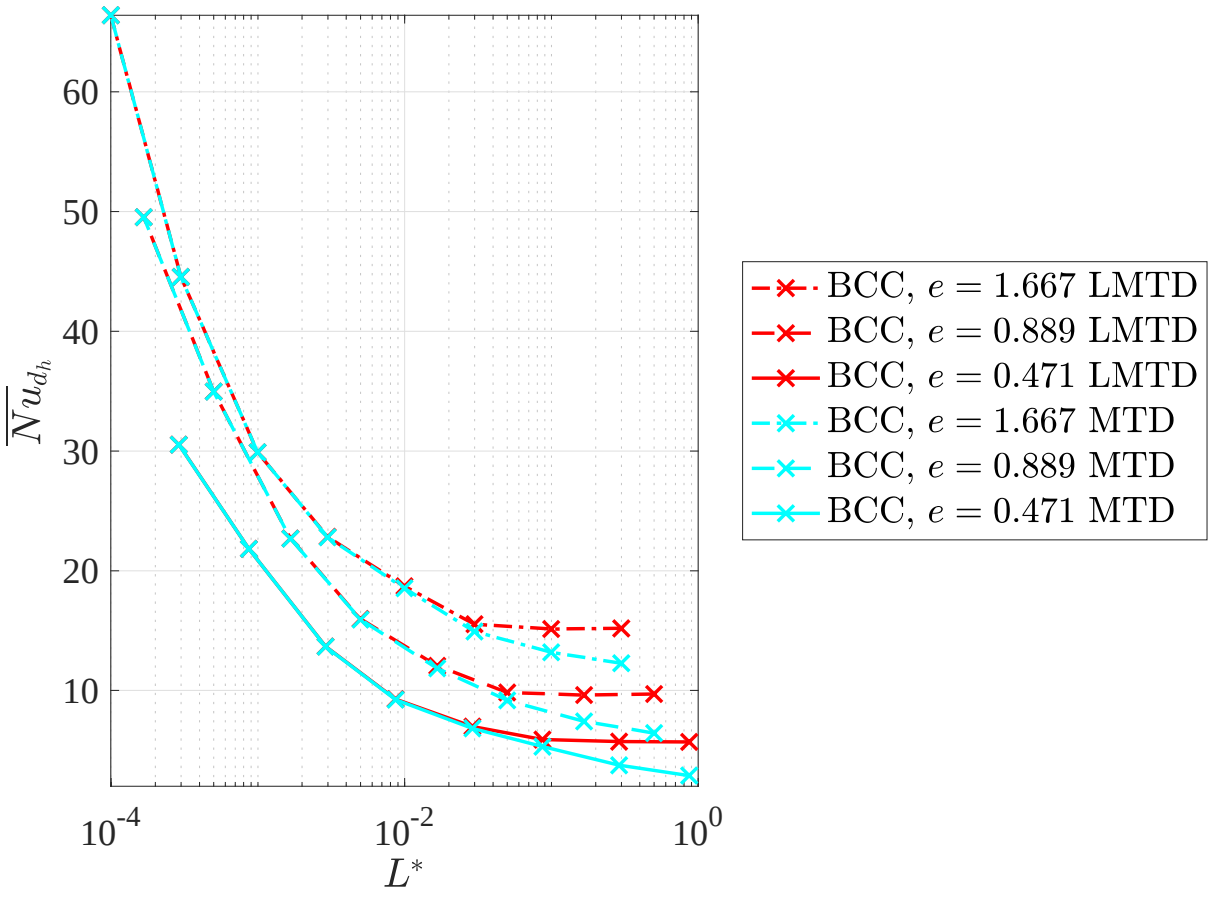


832

833

834 *Figure 12 2D Schematic illustration of the definition of inlet and outlet velocities (u_{in} and u_{out}), inlet*
835 *and outlet face normal (u_{in} and u_{out}) and particle surface heat flux q_h for analysis of a whole throat.*

836

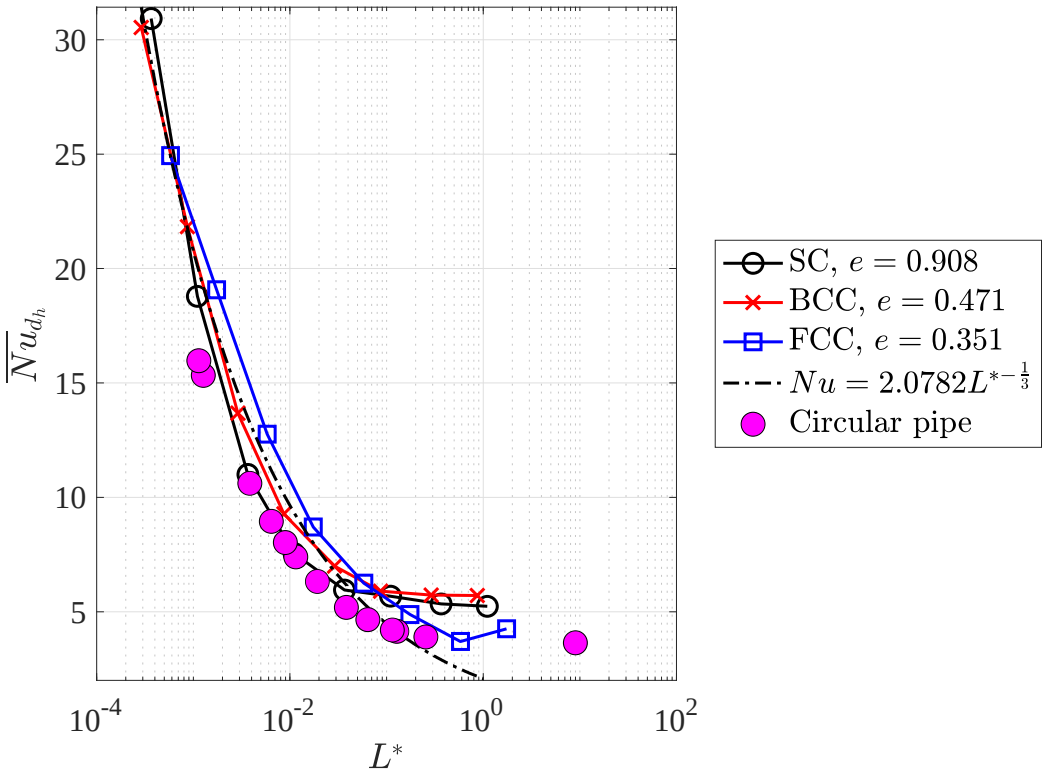


837

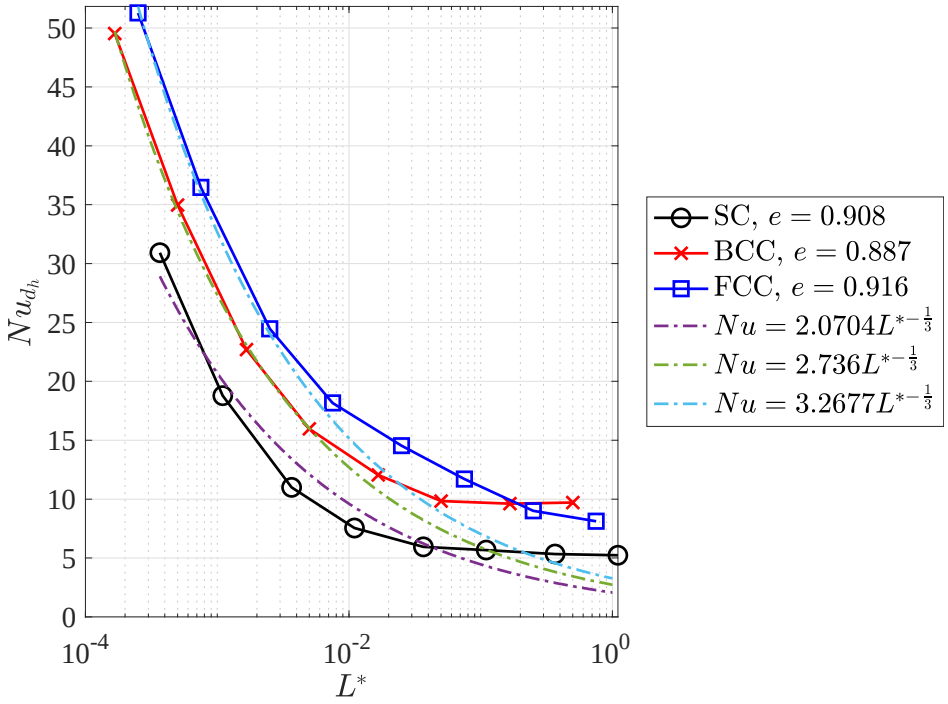
838

839 *Figure 13 Variation of $\overline{Nu_{FD}}$ with L^*: comparison between two definitions of θ (LMTD and MTD)*

840

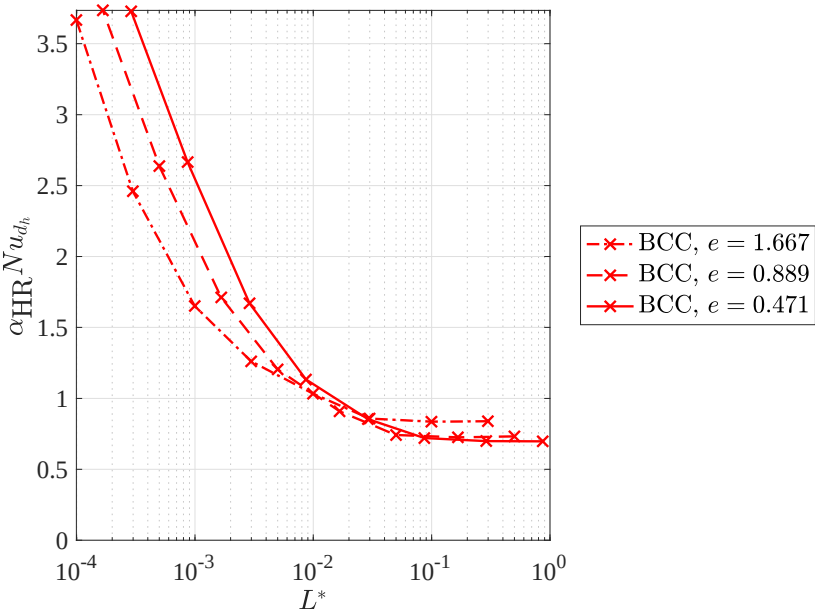


(a)

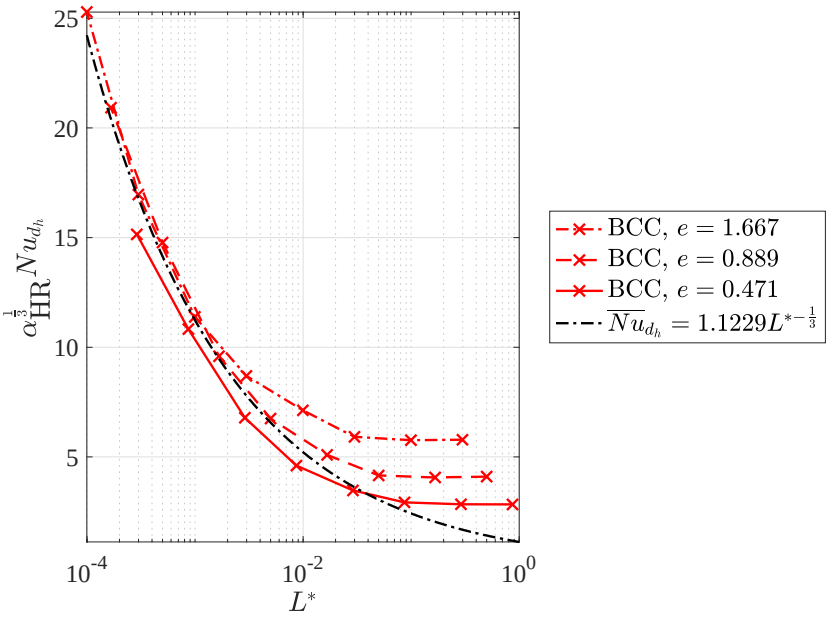


(b)

Figure 14 Variation of Nu_{dh} with L^*: (a) OpenFOAM data and best fit expression for the densest SC, BCC, FCC packings, and a circular pipe (Shah and London, 1978) (b). OpenFOAM data and best fit expressions for SC, BCC and FCC packings with a similar density

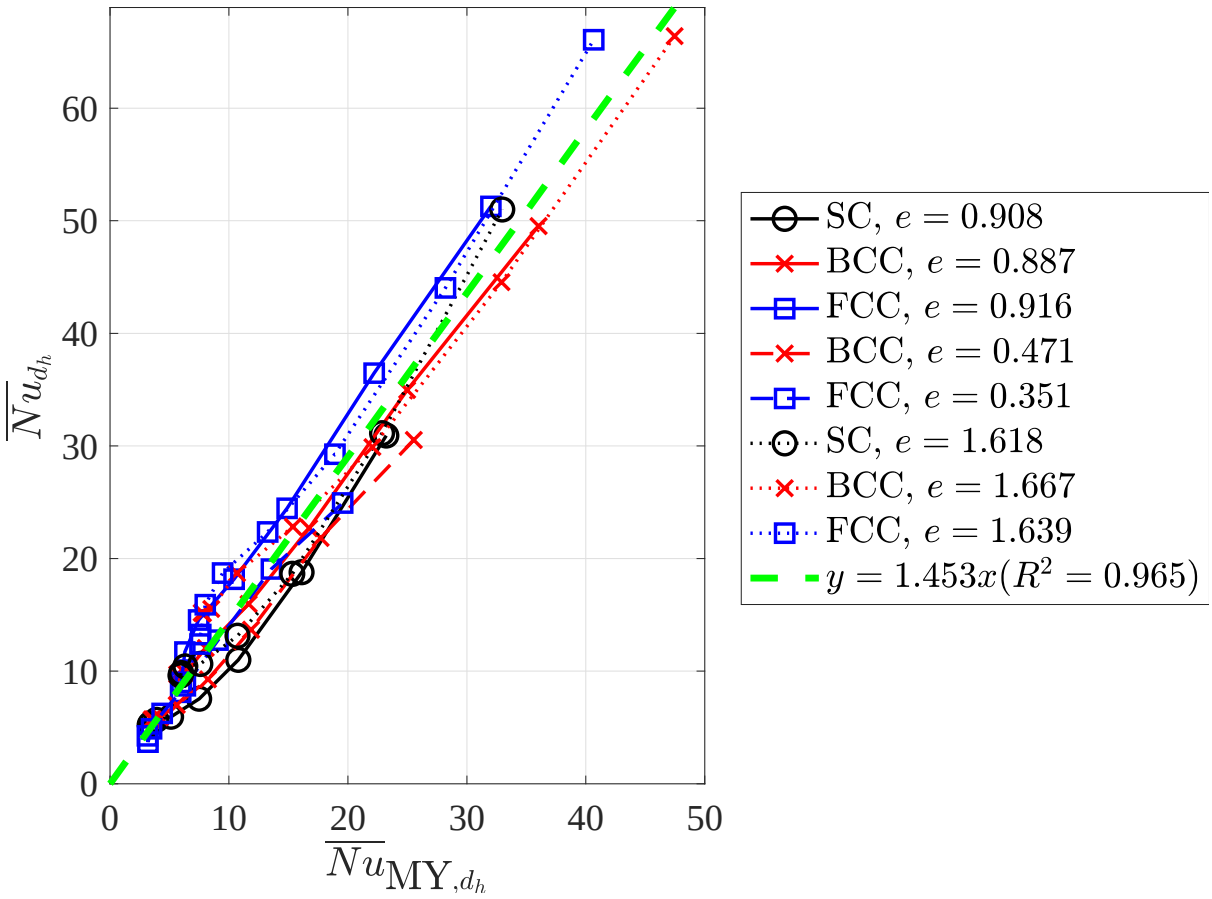


(a)



(b)

Figure 15(a) $\alpha_{HR} Nu_{d_h}$ versus L^* for the BCC packings with different void ratios. (b) $\alpha_{HR}^{1/3} Nu_{d_h}$ versus L^* for the BCC packings with different void ratios.



857

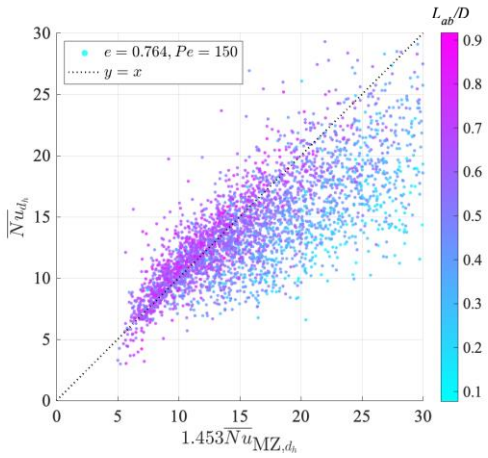
858

859 *Figure 16 Nu of throats in three types of regular packings with various void ratios and Nu predicted*

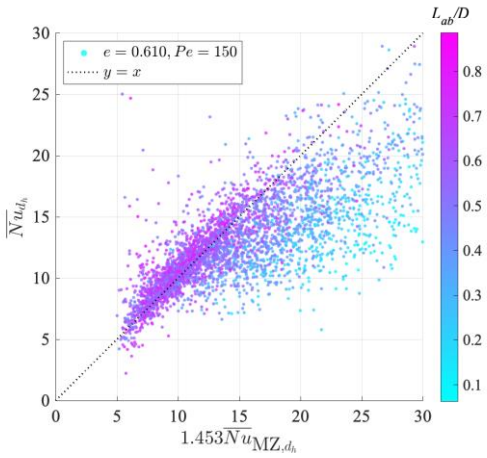
860 *by Eq. 34*

861

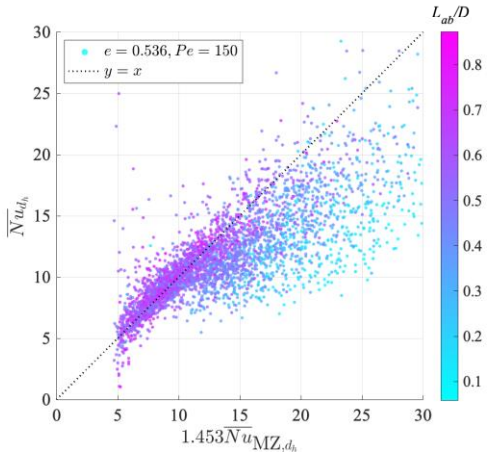
862



(a) e = 0.764



(b) e = 0.610



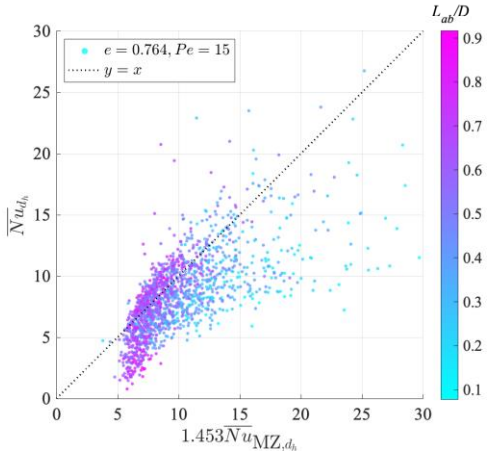
(c) e = 0.536

863

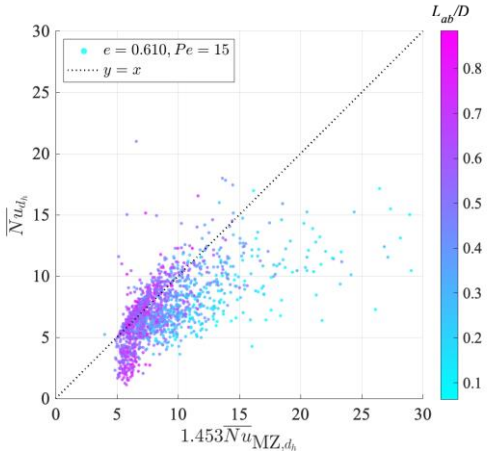
864 *Figure 17 Actual Nu and predicted Nu for Pe = 150.*

865

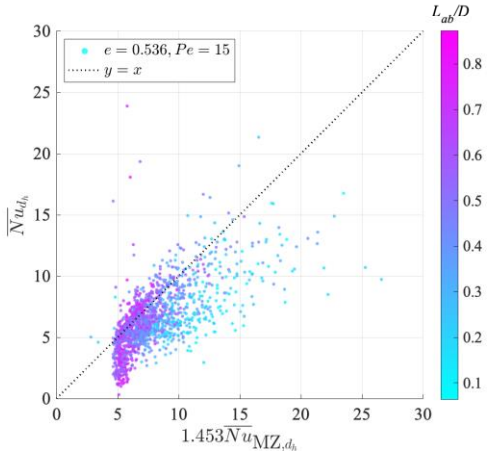
866



(a) e = 0.764



(b) e = 0.610



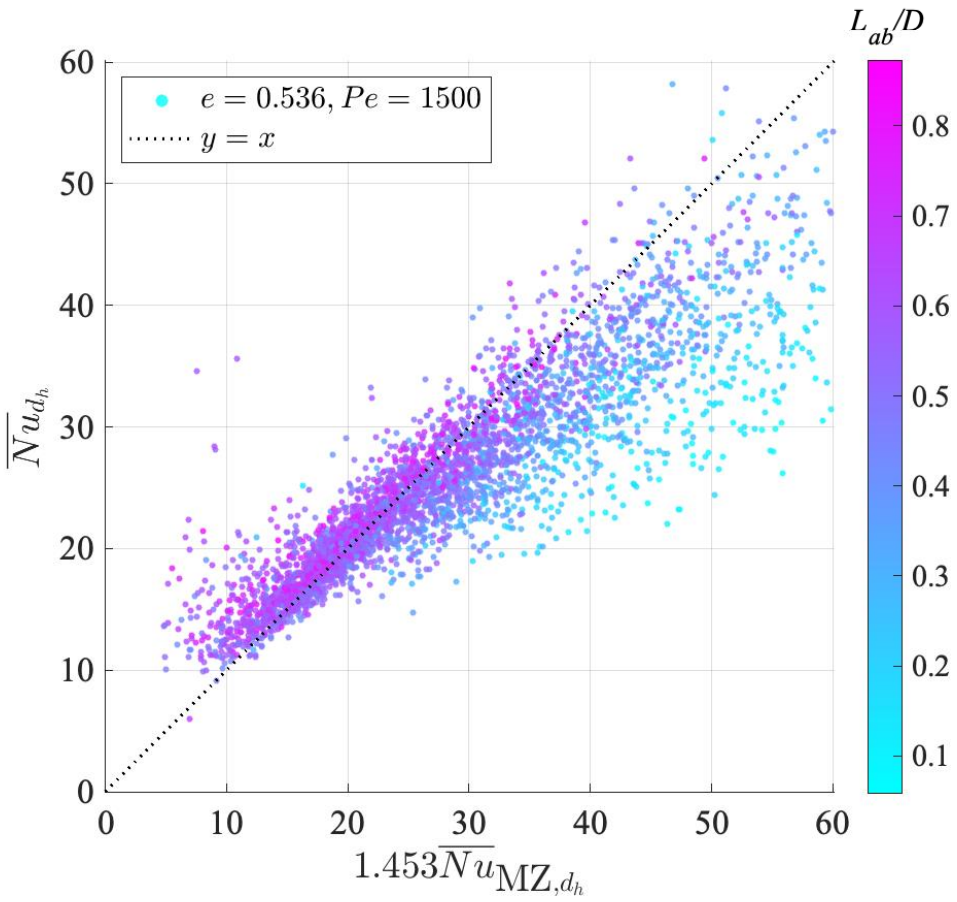
(c) e = 0.536

867

868 *Figure 18 Actual Nu and predicted Nu for Pe = 15.*

869

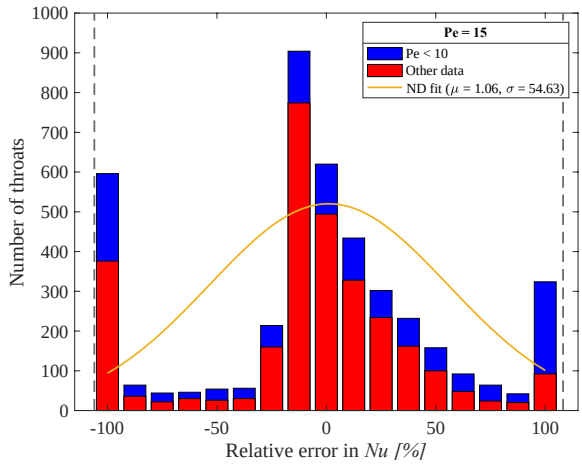
870



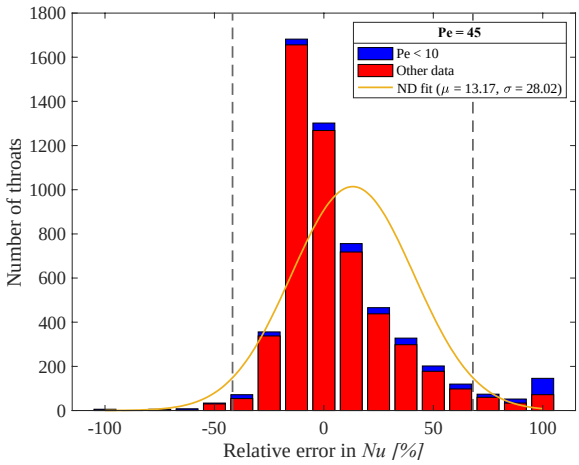
871

872 *Figure 19 Actual Nu and predicted Nu for Pe = 1500 and e = 0.536.*

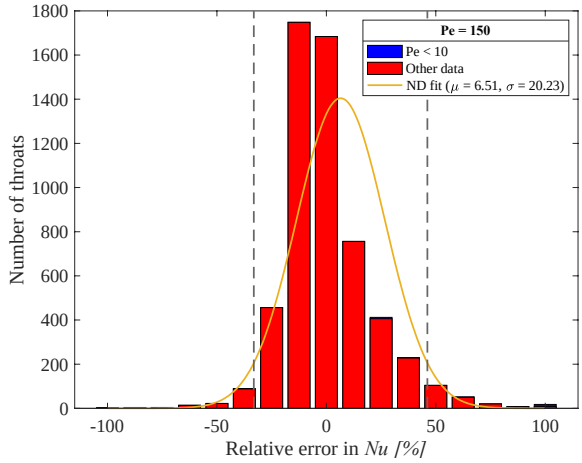
873



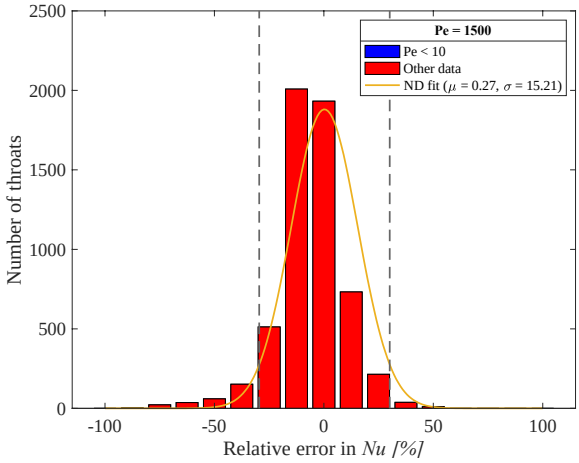
(a) Pe = 15



(b) Pe = 45

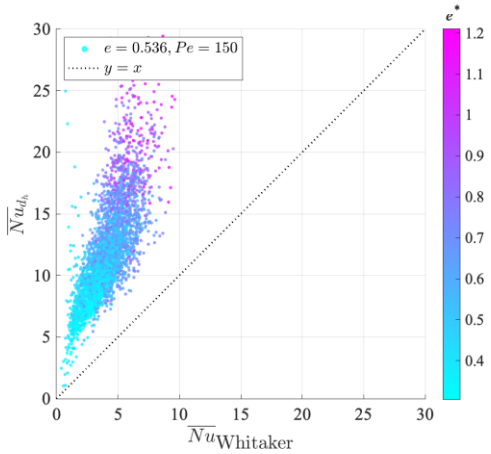


(c) Pe = 150

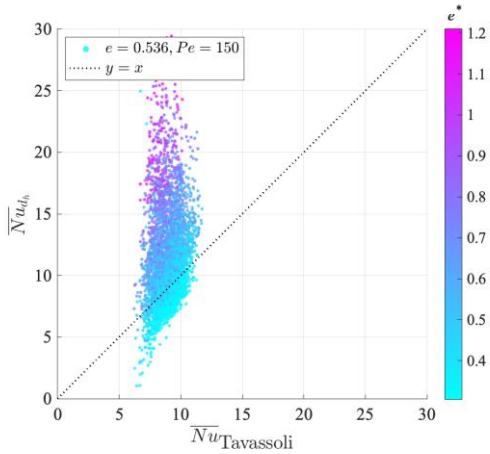


(c) Pe = 1500

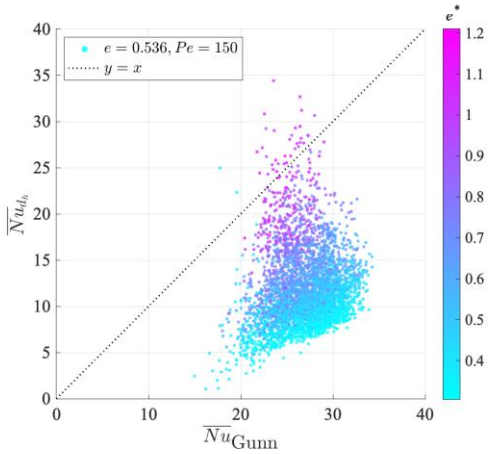
Figure 20 Histograms giving the numbers of throats with specific values of the relative error in the throat Nu for various Pe values with $e = 0.536$. "ND fit" stands for normal distribution fit. For each bin the number of pores is divided into pores with a local $Pe < 10$ (blue shading) and pores with a local $Pe \geq 10$ (red shading)



(a) Whitaker (1972)'s model



(b) Tavassoli et al. (2015)'s model



(c) Gunn (1978)'s model

881

882 *Figure B.1 Actual Nu and predicted Nu by existing models for Pe = 150 and e = 0.536.*

883

884 *Table 1 Influence of length of inlet and outlet regions on Nu and f for SC validation simulations*
885 *($D/ds_c = 50$)*

L_{in}	D	D	$2D$	$2D$
L_{out}	D	$2D$	D	$2D$
$Re = 0.7$	$Nu = 3.32$ $f = 235.2$	$Nu = 3.36$ $f = 235.1$	$Nu = 3.37$ $f = 233.6$	$Nu = 3.34$ $f = 233.5$
$Re = 7$	$Nu = 3.32$ $f = 24.4$	$Nu = 3.36$ $f = 24.4$	$Nu = 3.37$ $f = 24.3$	$Nu = 3.34$ $f = 24.2$

886

887

Table 2 Influence on mesh size (D/ds_c) on Nu and f (Pr=2.28, $L_{in} = D$, $L_{out} = D$)

D/ds_c	30	40	50	60
$Re = 0.7$	$Nu = 3.36$ $f = 227.7$	$Nu = 3.35$ $f = 229.9$	$Nu = 3.32$ $f = 235.2$	$Nu = 3.34$ $f = 235.9$
$Re = 7$	$Nu = 4.85$ $f = 23.7$	$Nu = 4.73$ $f = 23.8$	$Nu = 4.68$ $f = 24.4$	$Nu = 4.65$ $f = 24.5$

888

889

890

Table 3 Characteristics of lattice packings considered

	$D[mm]$	e	$L_{ab}[mm]$	$d_h = \frac{2}{3}De[mm]$	L_{ab}/D
SC	12.00	0.910	12.00	7.28	1.00
	10.80	1.620		11.66	1.11
BCC	12.00	0.470	4.90	3.76	0.41
	11.04	0.888		6.54	0.44
	9.84	1.666		10.93	0.50
FCC	12.00	0.350	7.35	2.80	0.61
	10.68	0.916		6.52	0.69
	9.60	1.638		10.48	0.77

894 *Table B.1. Nu values predicted by three models at Re = 0.1 and Pr = 1500 with a variety of*

895 *porosities.*

Porosity	0.3	0.35	0.4	0.45	0.5	0.55	0.6	0.65	0.7
Void ratio	0.43	0.54	0.67	0.82	1.00	1.22	1.50	1.86	2.33
Whitaker (1972)	3.75	3.75	3.75	3.75	3.75	3.75	3.75	3.75	3.75
Tavassoli et al. (2015)	9.44	8.69	8.00	7.37	6.79	6.27	5.80	5.40	5.04
Gunn (1978)	28.59	26.36	24.30	22.40	20.66	19.10	17.69	16.45	15.38

896

897